An Investigation of Possible Non-Standard Photon Statistics in a Free-Electron Laser

A DISSERTATION SUBMITTED TO THE GRADUATE DIVISION OF THE UNIVERSITY OF HAWAI‘I AT MĀNOA IN PARTIAL FULFILLMENT OF THE REQUIREMENTS FOR THE DEGREE OF

DOCTOR OF PHILOSOPHY
IN
PHYSICS

December 2019

By
Jeong-Wan Park

Dissertation Committee:
Eric Szarmes, chairperson
Jason Kumar
Gary Varner
Xerxes Tata
Marcus Tius
Kwang-Je Kim

I dedicate this dissertation to my mother, Mrs. Young-Min Ku.

Acknowledgements

First, I would like to express my sincerest appreciation to the previous committee chair, Professor John Madey, for introducing the topic to me. Prof. Madey was an inspiration to me.

I am grateful to Professor Eric Szarmes for serving as the committee chair, since Prof. Madey's passing in 2016 July. Prof. Szarmes also kindly served as the University of Hawaii at Manoa principal investigator of my research program funded by the US Department of Energy, and gave me helpful advice on the classical free-electron laser theory and quantum optics.

I am also grateful to Professors Jason Kumar, Gary Varner, Xerxes Tata, and Marcus Tius for serving as the committee members. Prof. Kumar gave me useful advice on the radiation theory, Prof. Varner gave me important comments on the photon counting experiment, Prof. Tata proofread the dissertation, and gave me much academic advice, and Prof. Tius kindly joined the committee although I could not ask in person.

I am also grateful to Professor Pui Lam for helping me to continue this research.

I am also grateful to Doctor William Fawley for modifying the GINGER code for this research.

I am also grateful to Professor Stanislav Baturin for academic discussions and encouragement.

I am also grateful to Doctor Ryan Lindberg for fruitful discussions which improved the dissertation noticeably. I have learned a lot from Dr. Lindberg.

I am also grateful to my friend, Professor Bosung Kim, for backing my research.

I am also grateful to my father, Mr. Dae-Heun Park, for support, which encouraged me greatly throughout my life.

Finally, I would like to appreciate Professor Kwang-Je Kim for thoughtfully arranging my visit to Argonne National Lab and UChicago to keep researching after Prof. Madey's passing. Without Prof. Kim's well-organized supervision finishing the dissertation would have been impossible.

Abstract

In an experiment performed some time ago, it was reported that the photon statistics of the 7th harmonic radiation of MARK III free-electron laser (FEL) was sub-Poissonian-neither Poissonian as expected from a coherent FEL output nor chaotic as expected from an incoherent radiation source. Whether FEL light exhibits such non-standard behavior is an important issue; if it does, our understanding of the FEL needs to be radically modified. This dissertation is an attempt to perform a comprehensive investigation of the conclusions of the above experiment. The investigation is performed from several perspectives-theoretical basis for the non-standard photon statistics as well as a re-examination of the data analysis of that experiment.

The observed behavior may arise from the quantum nature of the FEL dynamics. Therefore, first, we take a critical look at the experiment; we revisit the semiclassical radiation theory and the standard theory of FEL photon statistics of the fundamental mode starting from the noise, and then develop the simplest quantum extension of the classical theory of harmonic radiation production as driven by the fundamental mode. We include the cavity loss with a beam splitter model, and compute the photon statistics of the harmonic modes. We show that the statistics cannot be sub-Poissonian for any initial state of the electrons.

The main argument made from the experiment was that the Fano factor F (the ratio of photon number variance to the average photon number) was lower than the value expected from a Poissonian source and also exhibits a significantly different behavior from a chaotic source. If non-standard FEL dynamics are ruled out, the effect must be due to some features of photon detecting schemes which are difficult to study analytically. We have therefore performed a comprehensive simulation of the Fano factor measurement set-up, starting from the FEL simulation using the GINGER code, and photon-detection simulation incorporating photon clustering and the photon counter's dead time effect.

According to the re-examination, we find that the observed value of F could be explained within the standard FEL theory if one combines the detector dead time effect with photon clustering arising from the FEL gain. Therefore, we propose an improved experiment for a more definitive measurement of the FEL photon statistics.

Contents

List of Figures

List of Tables

Chapter 1

Introduction

1.1 Historical context

The free-electron laser (FEL) was first invented by John Madey [1] and subsequently demonstrated experimentally by his colleagues [2]. Although Madey's first invention was based on a quantum analysis, following development of relevant classical theories can explain most of the FEL phenomena. However, for the FEL photon statistics, as the influence of vacuum fluctuations of the radiation field is not negligible at all, we necessarily need a quantum theory to explain it.

The predictions of standard classical FEL theory for the intensity, angular, and spectral distribution of the radiation have generally been well confirmed by experiment [3]. However, the intensity fluctuations of the FEL which originate from quantum nature had not been measured well. Therefore, Chen and Madey measured the intensity fluctuations in the coherent spontaneous harmonic radiation (CSHR) generated by MARK III FEL (this experiment is referred to as Chen-Madey experiment in this dissertation) [3]. From the measurement, they claimed that the observed photon statistics is sub-Poissonian; they claimed that the observed intensity fluctuations were less than that predicted by the semiclassical radiation theory [3]. Chen and Madey argued that their observation constitutes the first experimental demonstration of the generation of non-classical light by a beam of free-electrons, and that their observation has fundamental consequences for our understanding of the physics responsible for the FEL operation [3]. They tried to find the theoretical explanation of the observation, but they could not find it, and concluded that the origin of observation should be related to some quantum nature of the radiation [4].

Prior to Chen-Madey experiment, there were some attempts to observe the photon statistics of radiation emitted by free-electrons. Teich et al. measured the fluctuations in the spontaneous undulator and bend-magnet radiation emitted by electrons circulating in a storage ring, and found a super-Poissonian light [5]. However, the measured intensity was so significant that the classical chaotic fluctuations dominated over the fluctuations originating from the quantum nature [6]. Therefore, the quantum fluctuations could not be measured accurately from the experiment. The radiation field intensity's fluctuations for the self-amplified spontaneous emission emitted by a high-gain radio frequency (RF) linac FEL were also measured by Hogan et al. [7]. However, whether the observed statistics reflects the fluctuations originating from the quantum nature accurately is not clear in the data analysis.

1.2 Structure of the dissertation

Whether FEL light exhibits non-standard behavior as Chen and Madey claimed from their observation is an important issue; if it does, our understanding of the FEL needs to be radically modified. However, this is the only experiment claiming a non-classical light emitted by free-electrons while standard FEL theory predicts that statistical distribution cannot be sub-Poissonian for the light measured in Chen-Madey experiment. Therefore, in this dissertation, we perform a comprehensive investigation of the conclusions of Chen-Madey experiment.

This dissertation is composed of seven chapters. Chapter 1 starts with the background of this dissertation, focusing on the fundamentals of the FEL and sub-Poissonian photon statistics. In Chapter 2, we investigate the FEL photon statistics predicted by the standard quantum FEL theory. We first revisit the semiclassical theory of radiation. Then we develop a quantum FEL oscillator formulation in the linear gain regime in which Chen-Madey experiment is done, using a standard high-gain quantum FEL theory and the beam splitter model describing cavity loss, and calculate the photon statistics of the fundamental mode. Then starting from a classical expression of harmonic radiation driven by the fundamental mode, we similarly develop a quantum oscillator model of the harmonic modes and calculate the photon statistics. We conclude that the photon statistics observed in Chen-Madey experiment cannot be sub-Poissonian according to the standard theory. In Chapter 3, we review the layout, result, and conclusion of Chen-Madey experiment in detail. In Chapter 4, we re-examine the analysis of Chen and Madey on the possibility of photon clustering in their measurement. In Chapter 5, we perform a comprehensive simulation of the Fano factor measurement set-up, starting from the FEL simulation using the GINGER code, and photon-detection simulation incorporating photon clustering and the photon counter's dead time effect. From the simulation, we conclude that the observed reduction of intensity fluctuations could be explained within the standard FEL theory if one combines the detector dead time effect with photon clustering arising from the FEL gain. In Chapter 6, we propose an improved experiment for a more definitive measurement of the FEL photon statistics. In Chapter 7, we summarize and conclude this dissertation. The main contents of this dissertation have been reported in Refs. [8] and [9].

1.3 Free-electron laser

The following contents of Section 1.3 are from Ref. [10]. Free-electron laser (FEL) is a laser source that produces coherent light from relativistic free-electrons as gain medium, instead of atomic or molecular material as other conventional lasers. In principle, an FEL can be operational at any wavelength, which is in contrast to other conventional lasers. FEL light can meet high peak and average power, and spatial and temporal coherence.

As shown in Fig. 1.1, an FEL can be operational in three different modes: 1) FEL oscillator, 2) Seeded FEL amplifier, and 3) Self-amplified spontaneous emission (SASE) FEL. In the 1) oscillator mode, which corresponds to the mode of Chen-Madey experiment, mirrors trap the radiation within the cavity. The basic components of the FEL oscillator are a relativistic electron beam, a periodic magnetic structure (undulator), and an optical resonator providing feedback and amplification. Therefore, the

field accumulates over many round-trips. This mode can be feasible as long as the mirrors of good quality are readily available. In the 2) amplifier mode, the FEL magnifies the radiation of which central frequency is close to the resonance frequency. In the 3) SASE mode, the FEL amplifies the spontaneous undulator radiation originating from shot noise, and thus produce semi-coherent radiation field without external source or mirrors. Most of the X-ray FEL operates in the SASE mode, as the mirrors' reflectivity at the wavelength is small.

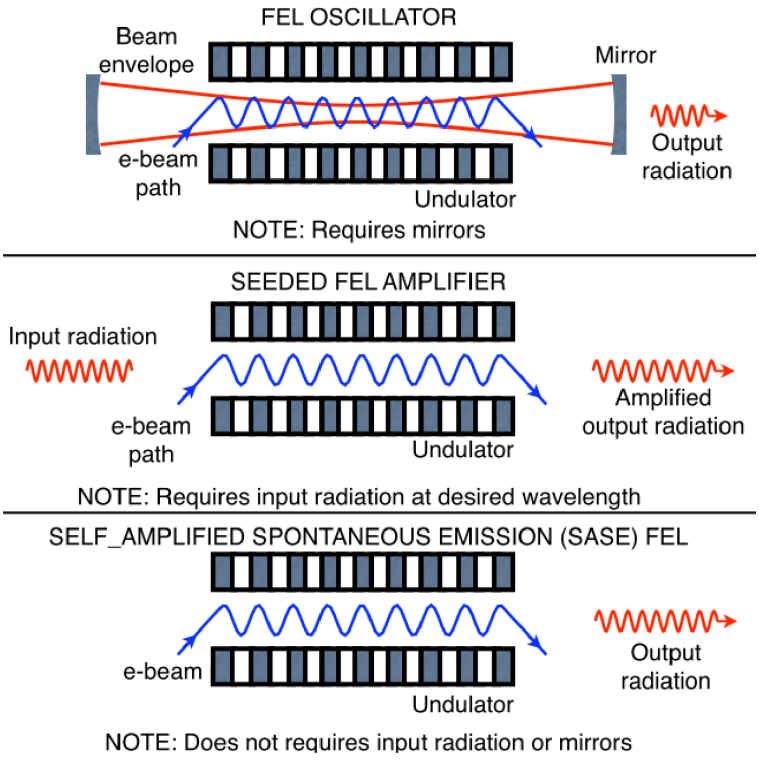

Figure 1.1: Three FEL modes (an edited version of a figure in [10], by Z. Huang).

1.3.1 Basic physics of an FEL oscillator

In an FEL oscillator, before an electron beam exits the electron gun, it travels longitudinally along the z-axis, and relativistic energy is delivered to the electron beam. When the emitted electron beam of relativistic longitudinal velocity passes through the periodic magnetic field created by the undulator, it oscillates within the transverse plane. Therefore it radiates spontaneously in the forward direction. The spontaneous optical beam co-propagates with the electron beam until it hits the downstream cavity mirror and gets reflected back to the cavity to interact with the subsequent electron pulses. Consequently, the electrons' bunching is created at the fundamental radiation wavelength and thus the radiation field is amplified, resulting in stimulated emission at wavelength given by:

$$\lambda_1 = \frac{\lambda_u}{2\gamma_r^2}(1 + \frac{K^2}{2}), \tag{1.1}$$

where λ_u and γ_r are the undulator period and the electron's resonance Lorentz factor respectively. Undulator deflection parameter K is defined:

$$K = \frac{eB_0\lambda_u}{2\pi mc}, \tag{1.2}$$

where B_0 is the amplitude of the magnetic field strength, e is the electron charge, and m is the electron mass.

1.3.2 High-gain FEL

In the low-gain FEL regime, we assume that the change of the radiation field originating from the photon-electron interaction is small and thus the radiation field is approximated to be constant within a single pass in the cavity. In contrast, in the high-gain FEL regime, the field cannot be considered as a constant during a single pass.

A high-gain FEL's time evolution can be described by the following three equations in a 1-D model:

$$\begin{aligned} \frac{d\theta_j}{d\hat{z}_j} &= \hat{\eta}_j, \\ \frac{d\hat{\eta}_j}{d\hat{z}} &= a e^{i\theta_j} + a^* e^{-i\theta_j}, \\ \frac{da}{d\hat{z}} &= -\langle e^{-i\theta_j} \rangle_\Delta. \end{aligned} \tag{1.3}$$

The variables of Eqn. (1.3) are the followings: $\hat{z} \equiv 2k_u \rho z$ is the scaled dimensionless longitudinal coordinate, $\hat{\eta}_j \equiv \frac{\eta_j}{\rho}$, where $\eta_j \equiv \frac{\gamma_j - \gamma_r}{\gamma_r}$. $a = \frac{\chi_1}{2k_u\rho^2} E$ is the dimensionless complex radiation field amplitude, where $\chi_1 \equiv \frac{eK[JJ]}{2\gamma_r^2 mc^2}$. $[JJ] = [JJ]_1$, where (h is the harmonic number)

$$[JJ]_h \equiv (-1)^{\frac{h-1}{2}} \{ J_{(h-1)/2}(h\xi) - J_{(h+1)/2}(h\xi) \}. \tag{1.4}$$

$\xi \equiv \frac{K^2}{4+2K^2}$, and $J_n(x)$ is the first kind Bessel function. $\langle e^{-i\theta_j} \rangle_\Delta \equiv \frac{1}{N_\Delta} \sum_{j \in \Delta} e^{-i\theta_j}$ is the local bunching factor (the $\langle \rangle_\Delta$ notation refers an average over N_Δ particles within the FEL electron beam slice at position z and phase θ; Δ is the set of electrons within the electron beam slice). The subscript j denotes the index of each electron. $\theta = (k_1 + k_u)z - \omega_1 t + \phi$ is the particle phase (ϕ is the radiation field's phase, k_1 and ω_1 are the wave-number and frequency of the fundamental mode, respectively, and k_u is the wave-number of the undulator). We introduce the dimensionless FEL Pierce parameter ρ:

$$\rho = \Big[\frac{1}{8\pi} \frac{I}{I_A} \Big(\frac{K[JJ]}{1 + K^2/2} \Big)^2 \frac{\gamma \lambda_1^2}{2\pi\sigma_x^2} \Big]^{1/3}; \tag{1.5}$$

$I_A = \frac{4\pi\epsilon_0 mc^3}{e} \simeq 17045A$ is the Alfén current, the electrons' transverse distribution is assumed to be Gaussian (σ_x is the RMS radius), and I is the electron beam current.

The frequency bandwidth $\frac{\Delta\omega}{\omega}$ is approximately $\sqrt{\rho/N_u}$ for the linear gain regime, ρ for the saturation regime, and $\frac{1}{2N_u}$ for the spontaneous undulator emission regime.

In the linear gain regime, the system of Eqn. (1.3) can be linearized in terms of three collective variables:

$$\begin{aligned} &a && \text{(field amplitude)} \\ &b = \langle e^{-i\theta_j} \rangle_\Delta && \text{(bunching factor)} \\ &P = \langle \hat{\eta}_j e^{-i\theta_j} \rangle_\Delta && \text{(collective momentum),} \end{aligned} \tag{1.6}$$

where the corresponding time evolution equations are given as the followings:

$$\frac{da}{d\hat{z}} = -b, \tag{1.7}$$

$$\frac{db}{d\hat{z}} = -iP, \tag{1.8}$$

$$\frac{dP}{d\hat{z}} = a. \tag{1.9}$$

Eqn. (1.7) implies that bunching produces coherent radiation, Eqn. (1.8) implies that modulation of electron energy causes density bunching, and Eqn. (1.9) implies that coherent radiation drives energy modulation.

1.3.3 Coherent spontaneous harmonic radiation

Coherent spontaneous harmonic radiation (CSHR) can be accompanied by the fundamental mode's radiation in a high-gain FEL. The generation of CSHR can be noticed from Eqs. (1.7-1.9). According to Eqn. (1.9), the fundamental field drives modulation of electron energy. Then, according to Eqn. (1.8), the modulation generates density bunching, not only at the scale of fundamental wavelength, but also at the scale of harmonic wavelengths. Then, according to Eqn. (1.7), the created harmonic bunching produces CSHR. The detailed quantitative description of CSHR is presented in Section 2.3.3.1.

1.4 Fano factor of photon statistics

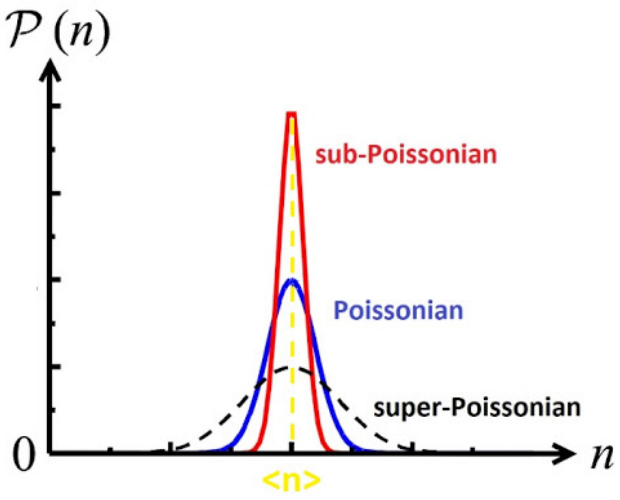

Figure 1.2: Three different types of photon statistics (edited from Ref. [11]).

The Fano factor F of photon statistics measures the ratio of variance to mean of the photon number distribution [12]:

$$F \equiv \frac{(\delta n)^2}{\langle n \rangle}. \tag{1.10}$$

Depending on the Fano factor value, the photon statistics can be divided into three different categories:

1. Poissonian ($F = 1$): coherent state, radiation by classical current with no intensity fluctuations
2. Super-Poissonian ($F > 1$): chaotic light
3. Sub-Poissonian ($F < 1$): non-classical light

1.5 Squeezed light and sub-Poissonian statistics

1.5.1 Characteristics of squeezed light

The following contents of Section 1.5.1 are from Ref. [13]. A single frequency mode of quantum electromagnetic field can be described by a pair of canonical conjugate variables. A commonly used set is the two quadrature components, where a_1 and a_2 are real and imaginary parts of the photon annihilation operator ($a = a_1 + ia_2$). The electric field can be expressed in terms of the quadratures as:

$$E = a_1 \cos(\omega t) + a_2 \sin(\omega t). \tag{1.11}$$

The uncertainty product of the two quadratures has a lower limit originating from the Heisenberg uncertainty principle:

$$\Delta a_1 \Delta a_2 \geq \frac{1}{4}. \tag{1.12}$$

From $[a, a^\dagger] = 1$, a_1 and a_2 can be shown to satisfy:

$$[a_1, a_2] = \frac{i}{2}. \tag{1.13}$$

For the coherent state, the probability distribution for a_1 and a_2 is the same as that of the vaccum state. Therefore, the uncertanties for the two quadratures become the same, and the uncertainty product of Eqn. (1.12) is minimized;

$$\Delta a_1 = \Delta a_2 = \frac{1}{2}. \tag{1.14}$$

In this case, the photon number distribution is Poissonian, and the Fano factor is one.

In contrast to the coherent state, the squeezed light is defined as the following [14]:

$$\Delta a_i < \frac{1}{2}, \text{ i=1 or 2.} \tag{1.15}$$

And if $\Delta a_j < \frac{1}{2}$ for a_j in phase with the electric field, such squeezed light is called amplitude-squeezed light. Some of the squeezed lights are also sub-Poissonian light; not every amplitude-squeezed light is sub-Poissonian light.

1.5.2 Generation of squeezed light

The commonly used mechanisms to generate squeezed light are four-wave mixing [15, 16] and optical parametric amplifier [17]. If FEL can be a source of the intense sub-Poissonian light, FEL can be used for research in quantum optics, particularly, in the high repetition-rate generation of the pure single photon states required for all optical quantum computing [18].

Chapter 2

The standard theory on FEL photon statistics

2.1 Light emitted by classical current

2.1.1 The semiclassical theory

First, we revisit the semiclassical radiation theory. The contents of Sections 2.1.1 and 2.1.2 are from Ref. [19].

We shall start by setting $P_m(T)$ to be a probability distribution for counting m photons during an observation time T. The photoelectric emission rate is proportional to the beam intensity, determined by the expectation value of the photon number operator. And the quantum-mechanical observable intensity is analogous to the period-averaged classical intensity. Let $p(t)dt$ be the probability that one photon is emitted during the time interval between t and $t + dt$. We assume that dt is so small that the probability that more than one photon is emitted during dt is negligible (independent photons), and that the quantum efficiency of photon counting is unity. Then we obtain:

$$p(t)dt = \bar{I}(t)dt, \tag{2.1}$$

where $\bar{I}(t)$ is a quantity proportional to the period-averaged classical intensity.

Let $P_m(t, T)$ be the probability that m photons are counted during the time interval between t and $t + T$. And let $t + t'$ be a time that lies within the interval between t and $t + T$, and let dt' be an infinitesimal time. There are only two different ways by which m photons can be registered during the time interval $(t, t + t' + dt')$ due to the following condition:

$$\lim_{dt\to 0} \frac{P_{m>1}(t, dt)}{P_1(t, dt)} = 0. \tag{2.2}$$

Either (1) m photons are counted between t and $t + t'$ and none is registered in the interval dt', with total probability

$$P_m(t, t')\{1 - p(t')dt'\}, \tag{2.3}$$

or (2) $m - 1$ photons are counted between t and $t + t'$ and one photon is registered in the interval dt', with total probability

$$P_{m-1}(t, t')p(t')dt'. \tag{2.4}$$

Then as Eqs. (2.3) and (2.4) are only available ways for counting m photons during the time interval $(t, t + t' + dt')$, the following equation can be obtained:

$$P_m(t, t' + dt') = P_m(t, t')\{1 - p(t')dt'\} + P_{m-1}(t, t')p(t')dt'. \tag{2.5}$$

Then, from the definition of differentiation and Eqs. (2.1) and (2.5), we can obtain the following:

$$\frac{dP_m(t, t')}{dt'} = \bar{I}(t')\{P_{m-1}(t, t') - P_m(t, t')\}. \tag{2.6}$$

Therefore, the probabilities $P_m(t, t')$ for the different values of m are related by a chain of differential equations. The first equation in the chain, for $m = 0$, can be obtained from Eqn. (2.6), by excluding the first term on the right hand side:

$$\frac{dP_0(t, t')}{dt'} = -\bar{I}(t')P_0(t, t'). \tag{2.7}$$

The probability $P_0(t, t')$ satisfies the boundary condition that no photons are counted in a time interval of zero,

$$P_0(t, 0) = 1. \tag{2.8}$$

With the boundary condition, the solution for Eqn. (2.7) becomes the following:

$$P_0(t, T) = exp\{-\bar{I}(t, T)T\}, \tag{2.9}$$

where $\bar{I}(t, T)$ is

$$\bar{I}(t, T) = \frac{1}{T}\int_t^{t+T} \bar{I}(t')dt'. \tag{2.10}$$

Then the remaining $P_m(t, T)$ for $m > 0$ can be successively obtained from Eqn. (2.6). The boundary condition complementary to Eqn. (2.8) for $m > 0$ is

$$P_m(t, 0) = 0. \tag{2.11}$$

Then, we can obtain the following solution:

$$P_m(t, T) = \frac{\{\bar{I}(t, T)T\}^m}{m!} exp\{-\bar{I}(t, T)T\}. \tag{2.12}$$

The probability $P_m(t, T)$ represents the statistical distribution of the photon count obtained in a series of experiments all of which begin at the same time t. However, in reality, it is usually possible to conduct only one counting measurement at a time, and successive counting periods sequentially follow rather than simultaneously. In some cases, $\bar{I}(t, T)$ can fluctuate, as for the chaotic light. Consequently, the measured photon-count distribution $P_m(T)$ is an average of $P_m(t, T)$ over a large number of different starting times t. Therefore, the following can be obtained:

$$P_m(T) = \langle P_m(t, T)\rangle = \left\langle \frac{\{\bar{I}(t, T)T\}^m}{m!} exp\{-\bar{I}(t, T)T\} \right\rangle, \tag{2.13}$$

where the angle brackets denote an average over t.

2.1.2 Photon statistics

Eqn. (2.13) can be applicable to any stationary light source, and for some special cases, it can be explicitly calculated. Consider first the simplest case in which $\bar{I}(t)$ is independent of t. Then, according to Eqn. (2.10), we can obtain the following:

$$\bar{I}(t,T) = \bar{I}. \tag{2.14}$$

Then Eqn. (2.13) becomes the following:

$$P_m(T) = \frac{\bar{n}^m}{m!} exp(-\bar{n}), \tag{2.15}$$

where $\bar{n} \equiv \bar{I}T$. The photon distribution $P_m(T)$ for the constant-intensity case is therefore the Poisson distribution. And the fluctuations of the Poisson distribution are known to be:

$$(\delta n)^2 = \bar{n}. \tag{2.16}$$

The fluctuations which occur for a beam of constant intensity are called *particle fluctuations*. They are due to the discrete nature of the photoelectric process (quantum nature), in which energy can be removed from the light beam only in whole photons. The particle fluctuations are intrinsic, irreducible feature of the photon counting experiment, as long as the probability of counting of more than one photon during the infinitesimal time interval is negligible. Light beams differ in the context to which they produce counting fluctuations in excess of Eqn. (2.16), but the particle fluctuations are invariably present.

Also for general $\bar{I}(t,T)$, the photon statistics can be computed. From Eqn. (2.13), the mean number of counted photon is:

$$\bar{n} = \sum_{m=0}^{\infty} m P_m(T) = \langle \bar{I}(t,T)T \rangle = \bar{I}T, \tag{2.17}$$

where $\bar{I} \equiv \langle \bar{I}(t,T) \rangle$ has been used, also with the normalization of the probability distribution,

$$\sum_{m=0}^{\infty} P_m(T) = 1. \tag{2.18}$$

In a similar way, the second moment of the distribution is:

$$\overline{n^2} = \sum_{m=0}^{\infty} m^2 P_m(T) = \langle \bar{I}(t,T)T \rangle + \langle (\bar{I}(t,T)T)^2 \rangle = \bar{n} + \langle (\bar{I}(t,T)T)^2 \rangle. \tag{2.19}$$

Then the variance of the distribution becomes:

$$(\delta n)^2 = \overline{n^2} - \bar{n}^2 = \bar{n} + T^2 \{ \langle \bar{I}(t,T)^2 \rangle - \bar{I}^2 \}. \tag{2.20}$$

The first term of the variance represents the particle fluctuations. The additional fluctuations represented by the second term in Eqn. (2.20) arise from the random variations in the instantaneous intensity and are known as *wave fluctuations*. The general result Eqn. (2.20) reduces to Eqn. (2.16) for the constant-intensity case. We shall rewrite Eqn. (2.20) as:

$$(\delta n)^2 = (\delta n)_Q^2 + (\delta n)_C^2, \tag{2.21}$$

where $(\delta n)_Q^2 = \bar{n}$ is the portion of variance originating from quantum nature (particle fluctuations), whereas $(\delta n)_C^2$ arises from classical fluctuations (wave fluctuations). In this dissertation, sub-script C represents the classical origin whereas Q represents the quantum origin.

2.1.3 Chaotic intensity fluctuations and photon statistics

$(\delta n)_C^2$ originating from the electrons' uniform (random) position distribution (chaotic light) can be explicitly calculated. The contents of Section 2.1.3 are from a similar calculation for the case when the counting time is significantly larger than σ_τ (defined below) in Ref. [20]. The field of chaotic light in the frequency domain is [10]:

$$E_\omega = \frac{E_0\sqrt{\pi}}{\sigma_\omega}\sum_{j=1}^{N_e} exp[-\frac{(\omega-\omega_r)^2}{4\sigma_\omega^2} + i\omega t_j]; \tag{2.22}$$

ω_r is resonant frequency, $\sigma_\omega = (2\sigma_\tau)^{-1}$ is the radiation bandwidth, $\sigma_\tau = \frac{t_{coh}}{2\sqrt{\pi}}$, and t_{coh} is the coherence time. Then the photon number is:

$$\bar{n}_C = \frac{4\pi\epsilon_0 c\lambda_r^2}{\hbar\omega_r}\int d\omega |E_\omega|^2. \tag{2.23}$$

Once E_ω of Eqn. (2.22) is plugged in Eqn. (2.23), it becomes:

$$\begin{aligned}\bar{n}_C &= \frac{4\pi\epsilon_0 c\lambda_r^2}{\hbar\omega_r}\frac{E_0^2\pi}{\sigma_\omega^2}\int d\omega \sum_{j,k} exp\Big[-\frac{(\omega-\omega_r)^2}{2\sigma_\omega^2} + i\omega(t_j-t_k)\Big] \\ &= \frac{4\pi\epsilon_0 c\lambda_r^2}{\hbar\omega_r}\frac{E_0^2\pi}{\sigma_\omega^2}\sqrt{2\pi}\sigma_\omega \sum_{j,k} exp\Big[-\frac{(t_j-t_k)^2}{8\sigma_\tau^2} + i\omega_r(t_j-t_k)\Big].\end{aligned} \tag{2.24}$$

The sum can be split into the diagonal terms and the off-diagonal terms:

$$\bar{n}_C = \frac{4\pi\epsilon_0 c\lambda_r^2}{\hbar\omega_r}\frac{E_0^2\pi}{\sigma_\omega^2}\sqrt{2\pi}\sigma_\omega\left\{N_e + \sum_{j\neq k,k} exp\Big[-\frac{(t_j-t_k)^2}{8\sigma_\tau^2} + i\omega_r(t_j-t_k)\Big]\right\}. \tag{2.25}$$

If the counting time T satisfies $T \gg \sigma_\tau$ or $T \ll \sigma_\tau$, which is assumed in this Section 2.1.3, the off-diagonal terms vanish. Therefore, we obtain the photon number as:

$$\bar{n}_C = \frac{4\pi\epsilon_0 c\lambda_r^2}{\hbar\omega_r}\frac{E_0^2\pi}{\sigma_\omega^2}\sqrt{2\pi}\sigma_\omega N_e. \tag{2.26}$$

Similarly, the second moment of the statistics becomes:

$$\begin{aligned}\overline{n^2}_C =& \left\{\frac{4\pi\epsilon_0 c\lambda_r^2}{\hbar\omega_r}\frac{E_0^2\pi}{\sigma_\omega^2}\sqrt{2\pi}\sigma_\omega\right\}^2 \\ &\times \sum_{j,k,l,m} exp\Big[-\frac{(t_j-t_k)^2+(t_l-t_m)^2}{8\sigma_\tau^2} + i\omega_r(t_j-t_k+t_l-t_m)\Big].\end{aligned} \tag{2.27}$$

The sum can be decomposed into three categories: 1) $j=k$, $l=m$, 2) $j=m$, $k=l$, $j\neq k$, and 3) remaining terms:

$$\begin{aligned}\overline{n^2}_C = &\left\{\frac{4\pi\epsilon_0 c\lambda_r^2}{\hbar\omega_r}\frac{E_0^2\pi}{\sigma_\omega^2}\sqrt{2\pi}\sigma_\omega\right\}^2\left\{N_e^2 + \sum_{j\neq k,k} exp\Big[-\frac{(t_j-t_k)^2}{4\sigma_\tau^2}\Big]\right. \\ &\left. + \sum_{\text{remaining}} exp\Big[-\frac{(t_j-t_k)^2+(t_l-t_m)^2}{8\sigma_\tau^2} + i\omega_r(t_j-t_k+t_l-t_m)\Big]\right\}.\end{aligned} \tag{2.28}$$

The last term again can be eliminated, as $T \gg \sigma_\tau$ or $T \ll \sigma_\tau$. Then $\overline{n^2}_C$ becomes:

$$\overline{n^2}_C = \bar{n}_C^2 \Big\{ 1 + \frac{1}{N_e^2} \sum_{j \neq k,k} exp\Big[- \frac{(t_j - t_k)^2}{4\sigma_\tau^2} \Big] \Big\}, \tag{2.29}$$

and the variance becomes:

$$(\delta n)_C^2 = \overline{n^2}_C - \bar{n}_C^2 = \bar{n}_C^2 \Big\{ \frac{1}{N_e^2} \sum_{j \neq k,k} exp\Big[- \frac{(t_j - t_k)^2}{4\sigma_\tau^2} \Big] \Big\}. \tag{2.30}$$

Then as t_j is uniformly distributed in the time interval of T, $(\delta n)_C^2$ becomes ($N_e \gg 1$):

$$\begin{aligned} (\delta n)_C^2 = \overline{n^2}_C - \bar{n}_C^2 &= \bar{n}_C^2 \frac{N_e(N_e - 1)}{T^2} \int dt dt' exp\Big[- \frac{(t - t')^2}{4\sigma_\tau^2} \Big] \\ &\simeq \frac{N_e^2}{T^2 \sigma_\omega^2} \{ \sqrt{\pi} T \sigma_\omega \mathrm{Erf}(T\sigma_\omega) + e^{-\sigma_\omega^2 T^2} - 1 \}. \end{aligned} \tag{2.31}$$

Therefore, $(\delta n)_C^2$ becomes:

$$(\delta n)_C^2 = \bar{n}_C^2 \frac{2\sqrt{\pi}\sigma_\tau}{T} \tag{2.32}$$

for $T \gg \sigma_\tau$, and

$$(\delta n)_C^2 = \bar{n}_C^2 \tag{2.33}$$

for $T \ll \sigma_\tau$. According to Eqn. (2.20), the light emitted by classical current cannot be sub-Poissonian.

2.2 Quantum efficiency of photon counting experiment

2.2.1 Beam splitter model

In a photon counting experiment, the quantum efficiency stems from reduction of the photon intensity which can be described as a random loss. This should be distinguished from other reduction factors which can be traced to a label of the photon operator (e.g., frequency).

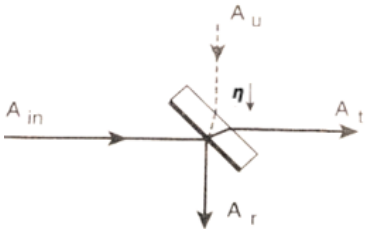

Figure 2.1: Beam splitter model (edited from Ref. [14]).

To quantum mechanically describe the quantum efficiency, we may employ the beam splitter model [11, 14], as shown in Fig. 2.1. The transmitted and reflected

classical radiation fields can be linked as the following (η is the quantum efficiency, and the subscripts infer the following: t denotes transmitted, r denotes reflected, in denotes input, and u denotes unused vacuum) [14]:

$$\begin{aligned} a_t e^{i\phi_t} &= \sqrt{1-\eta}\, a_{in} e^{i\phi_{in,t}} + \sqrt{\eta}\, a_u e^{i\phi_{u,t}}, \\ a_r e^{i\phi_r} &= \sqrt{\eta}\, a_{in} e^{i\phi_{in,r}} + \sqrt{1-\eta}\, a_u e^{i\phi_{u,r}}. \end{aligned} \tag{2.34}$$

From the energy conservation, we can obtain the relations between the phases as the following:

$$\begin{aligned} &|a_{in}|^2 + |a_u|^2 = |a_t|^2 + |a_r|^2 \\ &= (1-\eta)|a_{in}|^2 + \eta|a_u|^2 + \eta|a_{in}|^2 + (1-\eta)|a_u|^2 \\ &+ \sqrt{\eta(1-\eta)}[a_{in}a_u^*(e^{i(\phi_{in,t}-\phi_{u,t})} + e^{i(\phi_{in,r}-\phi_{u,r})}) + c.c.], \end{aligned} \tag{2.35}$$

which dictates the following:

$$e^{i(\phi_{in,t}-\phi_{u,t})} + e^{i(\phi_{in,r}-\phi_{u,r})} = 0. \tag{2.36}$$

Once we quantize the radiation field, from Eqn. (2.36), we can obtain the following commutation relations:

$$\begin{aligned} &[\mathfrak{a}_r, \mathfrak{a}_r^\dagger] = [\mathfrak{a}_t, \mathfrak{a}_t^\dagger] = 1, \\ &[\mathfrak{a}_r, \mathfrak{a}_t^\dagger] = 0. \end{aligned} \tag{2.37}$$

After passing the beam splitter, the output photon operator can be expressed as the following for the kth frequency component:

$$\mathfrak{a}_{r,k} e^{i\phi_{r,k}} = \sqrt{\eta_k}\,\mathfrak{a}_{in,k} e^{i\phi_{in,r,k}} + \sqrt{1-\eta_k}\,\mathfrak{a}_{u,k} e^{i\phi_{u,r,k}}, \tag{2.38}$$

and the initial state is the following:

$$|IN\rangle = \prod_k |in\rangle_k |0\rangle_{u,k}, \tag{2.39}$$

where $|in\rangle_k$ is the initial (prior to the beam splitter) photon state of the kth frequency mode.

2.2.2 Quantum efficiency's influence on the observed statistics

The photon operator becomes the following:

$$\mathfrak{n} = \sum_k \Big[\eta_k \mathfrak{n}_{in,k} + (1-\eta_k)\mathfrak{n}_{u,k} + \sqrt{(1-\eta_k)\eta_k}\big\{\mathfrak{a}_{in,k}^\dagger \mathfrak{a}_{u,k} e^{i(-\phi_{in,r,k}+\phi_{u,r,k})} + H.c.\big\}\Big]. \tag{2.40}$$

Consequently, the first two moments of the photon statistics become the following:

$$\langle IN|\mathfrak{n}|IN\rangle = \sum_k \eta_k \langle \mathfrak{n}\rangle_{in,k}, \tag{2.41}$$

$$
\begin{aligned}
\langle IN|\mathfrak{n}^2|IN\rangle &= \sum_{k,k'}\Big[\eta_k\eta_{k'}\langle IN|\mathfrak{n}_{in,k}\mathfrak{n}_{in,k'}|IN\rangle \\
&+ \sqrt{(1-\eta_k)\eta_k}\sqrt{(1-\eta_{k'})\eta_{k'}}\langle IN|\left\{\mathfrak{a}^\dagger_{in,k}\mathfrak{a}_{u,k}e^{i(-\phi_{in,r,k}+\phi_{u,r,k})}+H.c\right\}^2|IN\rangle\Big] \\
&= \sum_{k,k'}\Big\{\delta_{k,k'}\eta_k^2\langle\mathfrak{n}^2\rangle_{in,k}+(1-\delta_{k,k'})\langle\mathfrak{n}\rangle_{in,k}\langle\mathfrak{n}\rangle_{in,k'}\eta_k\eta_{k'} \\
&+ \delta_{k,k'}\sqrt{(1-\eta_k)\eta_k}\sqrt{(1-\eta_{k'})\eta_{k'}}\langle IN|\mathfrak{n}_{in,k}|IN\rangle\Big\} \\
&= \sum_k \eta_k^2(\langle\mathfrak{n}^2\rangle_{in,k}-\langle\mathfrak{n}\rangle^2_{in,k})+(\sum_k\eta_k\langle\mathfrak{n}\rangle_{in,k})^2+\sum_k(1-\eta_k)\eta_k\langle\mathfrak{n}\rangle_{in,k} \\
&= \sum_k \eta_k^2\langle(\delta\mathfrak{n})^2\rangle_{in,k}+\langle\mathfrak{n}\rangle^2_{in}+\sum_k(1-\eta_k)\eta_k\langle\mathfrak{n}\rangle_{in,k}.
\end{aligned}
\tag{2.42}
$$

Consequently, the variance becomes the following:

$$
\langle(\delta\mathfrak{n})^2\rangle_{out} = \sum_k \eta_k^2\langle(\delta\mathfrak{n})^2\rangle_{in,k}+\sum_k(1-\eta_k)\eta_k\langle\mathfrak{n}\rangle_{in,k}. \tag{2.43}
$$

If the the quantum efficiencies are fixed for the frequencies passed by the monochrometer as shown in Fig. 2.2, and the photon statistics are k independent for those passed frequencies, the observed Fano factor becomes the following:

$$
F_{out} = \eta F_{in} + (1-\eta), \tag{2.44}
$$

which means that the monochrometer's frequency selection does not affect F_{out}.

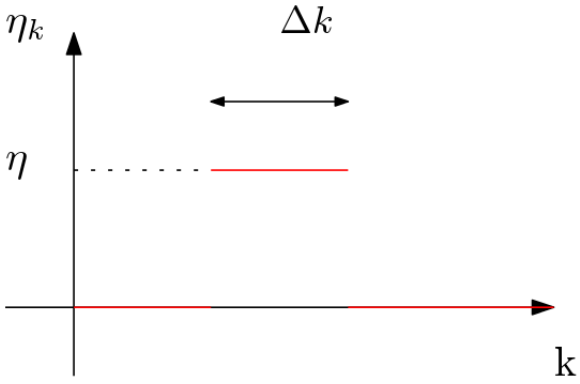

Figure 2.2: Constant quantum efficiencies for the frequencies passed by the monochrometer.

According to Eqn. (2.44), if $\eta \ll 1$, $F_{out} \simeq 1$ despite the actual value of F_{in}. Therefore, to definitively measure the Fano factor at the source, high η is required.

2.3 Quantum FEL theory

2.3.1 Oscillator in the linear gain regime

In Section 2.3, we will develop the quantum oscillator model of the fundamental mode, and explore its Fano factor of the photon statistics. The contents of Section 2.3.1 are from Ref. [10].

The easiest way to study the quantum effects of FEL is to quantize the FEL equations in the frequency domain, assuming that the radiation field is periodic over time T. This is valid as long as the radiation wavelength is much shorter than the length of electron beam. First, we start from the classical equations for the change of the scaled electron energy as follows ($\nu = \omega/\omega_1$):

$$\frac{d\hat{\eta}_j}{d\hat{z}} = \frac{\lambda_1}{cT}\sum_{\nu}(a_\nu e^{i\nu\theta_j} + c.c.). \tag{2.45}$$

The phase equation is $\frac{d\theta_j}{d\hat{z}} = \hat{\eta}_j$, and the Maxwell equation in frequency space is the following:

$$\Big(\frac{\partial}{\partial\hat{z}} + \frac{i\Delta\nu}{2\rho}\Big)a_\nu = -\frac{1}{N_\lambda}\sum_j e^{-i\nu\theta_j} = -\frac{cT}{\lambda_1}\frac{1}{N_e}\sum_j e^{-i\nu\theta_j}, \tag{2.46}$$

where $\Delta\nu \equiv \nu - h$ (h is the harmonic number), and N_λ and N_e are the total number of electrons in radiation wavelength and the bunch, respectively. Here, we associate a_ν with the quantum field operator $\mathfrak{a}_\nu$ defined such that $\mathfrak{a}_\nu^\dagger\mathfrak{a}_\nu$ is the number operator of photons with scaled frequency ν ($\mathfrak{a}_\nu^\dagger$ represents the Hermitian conjugate of $\mathfrak{a}_\nu$). Hence, $\mathfrak{a}_\nu^\dagger$ and $\mathfrak{a}_\nu$ are respectively the creation and annihilation operators of photon with frequency $\nu\omega_1$, and $\hbar\nu\omega_1\mathfrak{a}_\nu^\dagger\mathfrak{a}_\nu$ is the field energy operator of mode of ν. To relate the classical field a_ν with the quantum operator $\mathfrak{a}_\nu$, we write the classical expression for the field energy as the following:

$$\begin{aligned} U = \int d\omega T\frac{dP}{d\omega} &\to \frac{2\pi\lambda_1}{T}\sum_\nu \frac{\epsilon_0}{\pi c}(2\pi\sigma_x^2)\langle|E_\nu(z)|^2\rangle \\ &= \rho\gamma_r mc^2 N_e\Big(\frac{\lambda_1}{cT}\Big)^2\sum_\nu\langle|a_\nu(z)|^2\rangle. \end{aligned} \tag{2.47}$$

Hence, the appropriate definition infers the quantum association:

$$a_\nu \to \frac{cT}{\lambda_1}\sqrt{\frac{\hbar\omega}{N_e\rho\gamma_r mc^2}}\mathfrak{a}_\nu = \sqrt{\nu}c_q\mathfrak{a}_\nu, \tag{2.48}$$

where $c_q \equiv \frac{cT}{\lambda_1}\sqrt{\frac{q}{N_e}}$. Here we have introduced the quantum FEL parameter $q \equiv \frac{\hbar\omega_1}{\rho\gamma_r mc^2}$, which is the ratio of the characteristic photon energy to the energy bandwidth of the FEL. When $q \ll 1$ an electrons emits $\sim \frac{1}{q} \gg 1$ photons before falling out of the FEL bandwidth, and thus the FEL is in the classical regime (MARK III FEL is in the classical regime). On the other hand, when $q \gg 1$, even the electron's emission of a single resonant photon knocks an electron out of the amplification bandwidth, which corresponds to quantum regime.

The mapping of Eqn. (2.48) infers the following equal time commutation relations for the field operator:

$$[\mathfrak{a}_\nu(\hat{z}), \mathfrak{a}_{\nu'}^\dagger(\hat{z})] = \delta_{\nu,\nu'}. \tag{2.49}$$

And the quantum version of the Maxwell equation [Eqn. (2.46)] is

$$\Big(\frac{\partial}{\partial\hat{z}} + \frac{i\Delta\nu}{2\rho}\Big)\mathfrak{a}_\nu = -\frac{1}{\sqrt{\nu q N_e}}\sum_j e^{-i\nu\Theta_j}, \tag{2.50}$$

where Θ_j is the quantum operator corresponding to the particle phase θ_j. From the classical FEL Hamiltonian formulation, $\tau = -ct$ and $mc\gamma$ are canonical position-momentum pair whose Poisson bracket $\{\tau_j, mc\gamma_l\} = \delta_{j,l}$. This Poisson bracket corresponds to $\{\theta_j \equiv k_1\tau_j - (k_1+k_u)z, \hat{\eta}_l \equiv \frac{\gamma_l-\gamma_r}{\rho\gamma_r}\} = \frac{\omega_1}{\rho\gamma_r mc^2}\delta_{j,l}$. Then, from the correspondence between the classical Poisson bracket and quantum commutation ($\{A,B\} = C \rightarrow [A,B] = \frac{i}{\hbar}C$), we can find the quantum canonical momentum via the following association:

$$\hat{\eta} \rightarrow \frac{\hbar\omega_1}{\rho\gamma mc^2}\mathfrak{p} \equiv q\mathfrak{p}, \tag{2.51}$$

so that satisfies the following:

$$[\Theta_j, \mathfrak{p}_l] = i\delta_{j,l}. \tag{2.52}$$

Then, now we can write the quantum Hamiltonian for the FEL in 1-D as the following:

$$\mathcal{H} = \sum_{j=1}^{N_e}\Big[\frac{q}{2}\mathfrak{p}_j^2 + \frac{1}{\sqrt{\nu q N_e}}\sum_\nu (i\mathfrak{a}_\nu e^{i\nu\Theta_j} + h.c.)\Big] + \sum_\nu \frac{\Delta\nu}{2\rho}\mathfrak{a}_\nu^\dagger\mathfrak{a}_\nu. \tag{2.53}$$

The corresponding Heisenberg equations of motion become the followings:

$$\begin{aligned}
&\frac{d}{d\hat{z}}\mathfrak{a}_\nu = i[\mathcal{H},\mathfrak{a}_\nu] = -i\frac{\Delta\nu}{2\rho}\mathfrak{a}_\nu - \frac{1}{\sqrt{\nu q N_e}}\sum_j^{N_e} e^{-i\nu\Theta_j},\\
&\frac{d}{d\hat{z}}\Theta_j = i[\mathcal{H},\Theta_j] = q\mathfrak{p}_j,\\
&\frac{d}{d\hat{z}}\mathfrak{p}_j = i[\mathcal{H},\mathfrak{p}_j] = \sum_\nu \sqrt{\frac{\nu}{qN_e}}\big[\mathfrak{a}_\nu e^{i\nu\Theta_j} + \mathfrak{a}_\nu^\dagger e^{-i\nu\Theta_j}\big],
\end{aligned} \tag{2.54}$$

which is in accordance with the classical 1-D FEL equations [Eqs. (1.7)-(1.9)]. These equations can be linearlized in the linear gain regime. This starts with the introduction of the bunching factor operator:

$$\mathscr{B}_\nu = \frac{1}{\sqrt{\nu q N_e}}\sum_{j=1}^{N_e} e^{-i\nu\Theta_j}, \tag{2.55}$$

and then the Maxwell equation is expressed as the following:

$$\Big(\frac{\partial}{\partial\hat{z}} + i\frac{\Delta\nu}{2\rho}\Big)\mathfrak{a}_\nu = -\mathscr{B}_\nu. \tag{2.56}$$

The time-evolution of bunching becomes the following:

$$\frac{d}{d\hat{z}}\mathscr{B}_\nu = i[\mathcal{H},\mathscr{B}_\nu] = -\nu\mathscr{P}_\nu, \tag{2.57}$$

where the collective momentum is

$$\mathscr{P}_\nu = \frac{1}{2}\sqrt{\frac{q}{\nu N_e}}\sum_{j=1}^{N_e}(\mathfrak{p}_j e^{-i\nu\Theta_j} + e^{-i\nu\Theta_j}\mathfrak{p}_j). \tag{2.58}$$

Then, ignoring the non-resonant terms, we can obtain the time evolution equation for $\mathscr{P}_\nu$ as the following:

$$\begin{aligned}\frac{d}{d\hat{z}}\mathscr{P}_\nu = i[\mathcal{H},\mathscr{P}_\nu] &= \mathfrak{a}_\nu - i\frac{\nu q}{4}\frac{1}{\sqrt{\nu q N_e}}\sum_{j=1}^{N_e}(\mathfrak{p}_j^2 e^{-i\nu\Theta_j} + e^{-i\nu\Theta_j}\mathfrak{p}_j^2 + 2\mathfrak{p}_j e^{-i\nu\Theta_j}\mathfrak{p}_j) \\ &= \mathfrak{a}_\nu - i\frac{\nu q}{4}\frac{1}{\sqrt{\nu q N_e}}\sum_{j=1}^{N_e}(\nu^2 e^{-i\nu\Theta_j} + 4\mathfrak{p}_j e^{-i\nu\Theta_j}\mathfrak{p}_j).\end{aligned} \tag{2.59}$$

The $\mathfrak{p}_j e^{-i\nu\Theta_j}\mathfrak{p}_j$ term is non-linear as can be seen from the following:

$$\begin{aligned}&\frac{d}{d\hat{z}}(\mathfrak{p}_j e^{-i\nu'\Theta_j}\mathfrak{p}_j) = \frac{d\mathfrak{p}_j}{d\hat{z}}e^{-i\nu'\Theta_j}\mathfrak{p}_j + \mathfrak{p}_j e^{-i\nu'\Theta_j}\frac{d\mathfrak{p}_j}{d\hat{z}} + \mathfrak{p}_j\frac{d}{d\hat{z}}e^{-i\nu'\Theta_j}\mathfrak{p}_j \\ &= \sum_\nu \sqrt{\frac{\nu}{qN_e}}\big\{(\mathfrak{a}_\nu e^{i(\nu-\nu')\Theta_j} + \mathfrak{a}_\nu^\dagger e^{-i(\nu+\nu')\Theta_j})\mathfrak{p}_j + \mathfrak{p}_j(\mathfrak{a}_\nu e^{i(\nu-\nu')\Theta_j} + \mathfrak{a}_\nu^\dagger e^{-i(\nu+\nu')\Theta_j})\big\} \\ &+ \mathfrak{p}_j\int_0^1 ds e^{(1-s)(-i\nu'\Theta_j)}q\mathfrak{p}_j e^{s(-i\nu'\Theta_j)}\mathfrak{p}_j.\end{aligned} \tag{2.60}$$

Therefore, Eqn. (2.59) can be simplified as the following:

$$\frac{d}{d\hat{z}}\mathscr{P}_\nu = \mathfrak{a}_\nu - i\frac{\nu^3 q^2}{4}\mathscr{B}_\nu. \tag{2.61}$$

From Eqs. (2.56), (2.57), and (2.61), we can obtain the following differential equation for $\mathfrak{a}_\nu$:

$$\frac{d^3\mathfrak{a}_\nu}{d\hat{z}^3} + i\frac{\Delta\nu}{2\rho}\frac{d^2\mathfrak{a}_\nu}{d\hat{z}^2} + \frac{\nu^4 q^2}{4}\frac{d\mathfrak{a}_\nu}{d\hat{z}} + i\nu\Big(\frac{\nu^3 q^2\Delta\nu}{8\rho} - 1\Big)\mathfrak{a}_\nu = 0. \tag{2.62}$$

We set $\nu \to 1$ except in the detuning term, since $\Delta\nu \sim \rho \ll 1$. If we assume that $\mathfrak{a}_\nu$ is proportional to $e^{-i\mu\hat{z}}$, we can obtain the following cubic equation for μ:

$$\Big(\mu - \frac{\Delta\nu}{2\rho}\Big)\Big(\mu^2 - \frac{q^2}{4}\Big) = 1. \tag{2.63}$$

Hence, the photon operator as a function of $\hat{z}$ is given as the following:

$$\mathfrak{a}_1(\hat{z}) = g(\hat{z})\mathfrak{a}_1(0) + f(\hat{z})\mathscr{B}(0) + h(\hat{z})\mathscr{P}(0). \tag{2.64}$$

$g(\hat{z})$, $f(\hat{z})$, and $h(\hat{z})$ are defined as the followings:

$$\begin{aligned}g(\hat{z}) &\equiv \sum_\alpha g_\alpha(\hat{z}) \equiv \frac{1}{3}\sum_\alpha e^{-i\mu_\alpha\hat{z}}, \\ f(\hat{z}) &\equiv \sum_\alpha f_\alpha(\hat{z}) \equiv -i\sum_\alpha \Upsilon_\alpha e^{-i\mu_\alpha\hat{z}}, \\ h(\hat{z}) &\equiv \sum_\alpha h_\alpha(\hat{z}) \equiv -i\sum_\alpha \frac{\Upsilon_\alpha}{\mu_\alpha}e^{-i\mu_\alpha\hat{z}},\end{aligned} \tag{2.65}$$

where μ_α are the solutions of Eqn. (2.63), and $\Upsilon_\alpha \equiv \frac{\mu_\alpha}{(\mu_\alpha-\mu_\beta)(\mu_\alpha-\mu_\gamma)}$. And the solutions for $\mathscr{B}_\nu(\hat{z})$ and $\mathscr{P}_\nu(\hat{z})$ are the followings:

$$\begin{aligned}
\mathscr{B}_\nu(\hat{z}) &= \sum_\alpha \frac{\Upsilon_\alpha}{\mu_\alpha}\Big[i\mathfrak{a}_\nu(0) + \mu_\alpha\Big(\mu_\alpha + \frac{\Delta\nu}{2\rho}\Big)\mathscr{B}_\nu(0) + \Big(\mu_\alpha + \frac{\Delta\nu}{2\rho}\Big)\mathscr{P}_\nu(0)\Big]e^{-i\mu_\alpha\hat{z}}, \\
\mathscr{P}_\nu(\hat{z}) &= \sum_\alpha \Upsilon_\alpha\Big[i\mathfrak{a}_\nu(0) + \frac{1}{\mu_\alpha}\Big\{1 + \frac{q^2}{4}\Big(\mu_\alpha + \frac{\Delta\nu}{2\rho}\Big)\Big\}\mathscr{B}_\nu(0) + \Big(\mu_\alpha + \frac{\Delta\nu}{2\rho}\Big)\mathscr{P}_\nu(0)\Big]e^{-i\mu_\alpha\hat{z}}.
\end{aligned} \tag{2.66}$$

From Eqn. (2.64), if we define the following quantum operator ($\hat{L}_u \equiv 2k_u\rho L_u$, where L_u is the length of undulator),

$$\mathcal{F} \equiv f(\hat{L}_u)\mathscr{B}(0) + h(\hat{L}_u)\mathscr{P}(0), \tag{2.67}$$

neglecting the cavity loss, the fundamental field's operator at the end of $(n+1)$th cavity round-trip can be related to that of the nth cavity round-trip as the following [$g \equiv g(\hat{L}_u)$] [21]:

$$\mathfrak{a}_{1,n+1} = g\mathfrak{a}_{1,n} + \mathcal{F}_n, \tag{2.68}$$

where $\mathcal{F}_n$ is the $\mathcal{F}$ for the fresh electron beam at the nth cavity round-trip.

2.3.2 Photon statistics of the fundamental mode

We incorporate cavity loss using the beam splitter model (Section 2.2.1) generalized to the hth harmonic mode. Then, we obtain the quantum iterative relation:

$$\mathfrak{a}_{1,n+1} = g\sqrt{\eta_1}e^{i\phi_{1,n}}\mathfrak{a}_{1,n} + g\sqrt{1-\eta_1}e^{i\phi_{1,u,n}}\mathfrak{a}_{1,u,n} + \mathcal{F}_n. \tag{2.69}$$

Note that the commutation relation $[\mathfrak{a}_{1,n}, \mathfrak{a}_{1,n}^\dagger] = 1$ is preserved. Solving the recursion relation, we obtain

$$\mathfrak{a}_{1,n} = (g\sqrt{\eta_1})^{n-1}e^{i\Phi_{1,1}}\mathfrak{a}_{1,1} \quad + \sum_{j=1}^{n-1}(g\sqrt{\eta_1})^{n-j-1}e^{i\Phi_{1,j+1}} \quad \Big[\mathcal{F}_j + g\sqrt{1-\eta_1}e^{i\phi_{1,u,j}}\mathfrak{a}_{1,u,j}\Big], \tag{2.70}$$

where $\Phi_{h,j} \equiv \sum_{k=j}^{n-1}\phi_{h,k}$. The expectation values of the first two moments of the photon number operator become:

$$\langle\mathfrak{n}\rangle_{1,n} = \sum_{j,k=1}^{n-1}(|g|\sqrt{\eta_1})^{2(n-1)-(j+k)}\langle\mathcal{F}'^\dagger_{n_j}\mathcal{F}'_{n_k}\rangle, \tag{2.71}$$

$$\begin{aligned}
\langle\mathfrak{n}^2\rangle_{1,n} = {} & \frac{(|g|^2\eta_1)^{n-1}(|g|^2-1) - |g|^2(1-\eta_1)}{|g|^2\eta_1 - 1}\langle\mathfrak{n}\rangle_{1,n} \\
& + \sum_{j,k,l,m=1}^{n-1}(|g|\sqrt{\eta_1})^{4(n-1)-(j+k+l+m)}\langle\mathcal{F}'^\dagger_{n_j}\mathcal{F}'_{n_k}\mathcal{F}'^\dagger_{n_l}\mathcal{F}'_{n_m}\rangle,
\end{aligned} \tag{2.72}$$

where $\mathcal{F}'_{n_j} \equiv e^{i[\Phi_{1,j+1}-j\mathrm{Arg}(g)]}\mathcal{F}_j$. One can show that the Fano factor of the hth harmonic mode after the nth cavity round-trip, $F_{h,n}$, satisfies the following for $h = 1$:

$$F_{1,n} = \frac{\{(|g|^2\eta_1)^{n-1} - 1\}(|g|^2 - 1)}{|g|^2\eta_1 - 1} + \frac{\langle(\delta\mathfrak{A}_n)^2\rangle}{\langle\mathfrak{n}_1\rangle_n} + 1 \geq 1, \tag{2.73}$$

provided $|g|^2 \geq 1$. Therefore, the photon statistics is not sub-Poissonian for any initial state of the electrons. For completeness, we also include the expression for the Hermitian operator $\mathfrak{A}_n$:

$$\mathfrak{A}_n = \sum_{j,k=1}^{n-1} (|g|\sqrt{\eta_1})^{2(n-1)-(j+k)} \mathcal{F}'^{\dagger}_{n_j} \mathcal{F}'_{n_k}. \tag{2.74}$$

2.3.2.1 Minimum noise state of electrons

The Fano factor can be explicitly computed if the initial electrons are in the minimum noise state $|\Psi\rangle$, defined as that which is annihilated by the Hermitian conjugate of $\mathcal{F}_n$ [10]:

$$\mathcal{F}_n^{\dagger}|\Psi\rangle = 0. \tag{2.75}$$

In this case, the first two moments of the photon statistics become the followings:

$$\begin{aligned}
\langle\mathfrak{n}\rangle_{1,n} &= \sum_{j,k=1}^{n-1} (|g|\sqrt{\eta_1})^{2(n-1)-(j+k)} \langle\mathcal{F}'^{\dagger}_{n_j}\mathcal{F}'_{n_k}\rangle = (|g^2| - 1)\sum_{j=1}^{n-1}(|g|^2\eta_1)^{n-j-1} \qquad (2.76)\\
&= \frac{(|g|^2 - 1)\{(|g|^2\eta_1)^{n-1} - 1\}}{|g|^2\eta_1 - 1},\\
\langle\mathfrak{n}^2\rangle_{1,n} &= \frac{(|g|^2\eta_1)^{n-1}(|g|^2 - 1) - |g|^2(1 - \eta_1)}{|g|^2\eta_1 - 1}\langle\mathfrak{n}\rangle_{1,n} \qquad (2.77)\\
&+ \sum_{j,k,l,m=1}^{n-1} (|g|\sqrt{\eta_1})^{4(n-1)-(j+k+l+m)} \langle\mathcal{F}'^{\dagger}_{n_j}\mathcal{F}'_{n_k}\mathcal{F}'^{\dagger}_{n_l}\mathcal{F}'_{n_m}\rangle\\
&= (1 + \langle\mathfrak{n}\rangle_{1,n})\langle\mathfrak{n}\rangle_{1,n} + \langle\mathfrak{n}\rangle_{1,n}^2 = 2\langle\mathfrak{n}\rangle_{1,n}^2 + \langle\mathfrak{n}\rangle_{1,n}.
\end{aligned}$$

Therefore, we can obtain the following expression of Fano factor:

$$F_{1,n} \equiv \frac{\langle(\delta\mathfrak{n}_1)^2\rangle_n}{\langle\mathfrak{n}_1\rangle_n} = 1 + \langle\mathfrak{n}_1\rangle_n, \tag{2.78}$$

which is equal to that of a chaotic light.

The following contents of Section 2.3.2.1 (except the last paragraph) are from Ref. [10]. The wave function of the minimum noise state can be explicitly calculated as shown below. In the classical regime ($q \ll 1$), as the quantum effects for $\mathcal{F}$ are small as shown below, we can write the quantum phase variable at $\hat{z} = 0$ as

$$\Theta_j(0) = \theta_j^c + \tilde{\Theta}_j, \tag{2.79}$$

where θ_j^c is a c-number denoting the initial classical position while $\tilde{\Theta}_j$ is the quantum correction that will be treated as a small quantity. Then according to Eqs. (2.55) and

(2.58), we can obtain the approximated $\mathscr{B}(0)$ and $\mathscr{P}(0)$ as the followings:

$$\begin{aligned}\mathscr{B}(0) &\simeq \frac{i}{\sqrt{qN_e}}\sum_{j=1}^{N_e} e^{-i\theta_j^c}(1-i\tilde{\Theta}_j),\\ \mathscr{P}(0) &\simeq \sqrt{\frac{q}{N_e}}\sum_{j=1}^{N_e} e^{-i\theta_j^c}\mathfrak{p}_j.\end{aligned} \tag{2.80}$$

In the high-gain limit ($|g(\hat{z})|^2 \gg 1$), for $\mathcal{F}(\hat{z})$, only the growing solution with μ_3 is dominant, resulting in $f \to f_3 = \frac{-ie^{-i\mu_3\hat{z}}}{\mu_3}$ and $h \to h_3 = \frac{-ie^{-i\mu_3\hat{z}}}{\mu_3^2}$ for Eqn. (2.65). Then, $\mathcal{F}(\hat{z})$ becomes the following:

$$\begin{aligned}\mathcal{F} = \mathcal{F}_C + \mathcal{F}_Q; \qquad \mathcal{F}_C &= -\frac{e^{-i\mu_3\hat{z}}}{3\mu_3\sqrt{qN_e}}\sum_{j=1}^{N_e} e^{-i\theta_j^c}\\ \mathcal{F}_Q &= -\frac{e^{-i\mu_3\hat{z}}}{3\mu_3\sqrt{qN_e}}\sum_{j=1}^{N_e} e^{-i\theta_j^c}\Big(\tilde{\Theta}_j + \frac{iq}{\mu_3}\mathfrak{p}_j\Big);\end{aligned} \tag{2.81}$$

the $\mathcal{F}$ is divided into a sum of a purely classical part $\mathcal{F}_C$ and the remaining part incorporating the quantum effects, $\mathcal{F}_Q$. Assuming that classically the electrons are uniformly (randomly) distributed, $\mathcal{F}_C = 0$, the condition of Eqn. (2.75) implies the following:

$$\mathcal{F}_Q^\dagger|\Psi\rangle = 0. \tag{2.82}$$

This implies the following for each electron:

$$\Big(\tilde{\Theta}_j - \frac{iq}{\mu_3^*}\mathfrak{p}_j\Big)|\Psi\rangle = 0. \tag{2.83}$$

As Θ_j and $\mathfrak{p}_j$ are conjugate operators, $\mathfrak{p}_j = -i\frac{\partial}{\partial\tilde{\theta}}$, and the normalized quantum wavefunction satisfying Eqn. (2.83) becomes the following:

$$\psi(\tilde{\theta}_j) = \frac{1}{\sqrt[4]{2\pi q}}\exp\Big(\frac{\mu_3^*\tilde{\theta}_j^2}{2q}\Big) = \frac{1}{\sqrt[4]{2\pi q}}\exp\Big(-\frac{1+\sqrt{3}i}{4q}\tilde{\theta}_j^2\Big). \tag{2.84}$$

Therefore, $|\psi(\tilde{\theta}_j)|^2$ is a Gaussian function centered at zero with RMS width of $\sqrt{q}$. Then, as we assume that the FEL is in the classical regime, electrons are uniformly distributed with little uncertainty in the position. To investigate the quantum phase space distribution, we can obtain the Wigner function:

$$W(\tilde{\theta},p) = \int d\xi\psi^*\Big(\tilde{\theta}+\frac{\xi}{2}\Big)\psi\Big(\tilde{\theta}-\frac{\xi}{2}\Big)e^{-i\xi p} = \exp\Big(-\frac{2}{q}\tilde{\theta}^2 - 2\sqrt{3}\tilde{\theta}p - 2qp^2\Big). \tag{2.85}$$

Due to the cross term of p and $\tilde{\theta}$, this distribution is a correlated Gaussian distribution in phase space, with the 1σ curve given by the rotated ellipse described by

$$\frac{4}{q}(\tilde{\theta}^2 + q\sqrt{3}\tilde{\theta}p + q^2p^2) = 1. \tag{2.86}$$

Therefore, for the wave function in p space, $|\phi(p_j)|^2$ has the RMS width of $\frac{1}{\sqrt{q}}$. $\mathcal{F}_Q$ is proportional to $\left(\tilde{\Theta}_j + \frac{iq}{\mu_3}\mathfrak{p}_j\right)$ of which width proportional to $\sqrt{q}$. Therefore, for $\mathcal{F}_Q$ and $\mathcal{F}_C$, the quantum effects are small compared to the classical electrons' distribution when $\sqrt{q} \ll 1$, which justifies the approximation used to obtain Eqn. (2.80) provided that $\sqrt{q} \ll 1$. If we keep the terms proportional to $\mathfrak{p}_j\tilde{\Theta}_j$ or $\tilde{\Theta}_j\mathfrak{p}_j$ in Eqn. (2.80), we face the following additional terms for Eqn. (2.83):

$$-\frac{iq}{\mu_3^*}\Big(1 + 2\frac{\mu_3^*\tilde{\theta}_j^2}{q}\Big)\exp\big(\frac{\mu_3^*\tilde{\theta}_j^2}{2q}\big)\psi(\tilde{\theta}_j) = 0; \tag{2.87}$$

considering the width of $|\psi(\theta_j)|^2$ or $|\phi(p_j)|^2$, Eqn. (2.87) is one order higher than Eqn. (2.83) in terms of $\sqrt{q}$ and thus is negligible.

In summary, provided that electrons are uniformly distributed ($\mathcal{F}_C = 0$), for the electrons' quantum state satisfying $\mathcal{F}^\dagger|\Psi\rangle = 0$ in the classical regime, although the corresponding wave function's width in the position space is much less than the radiation wavelength, as θ_j^c is randomly distributed, the electrons' radiation can still be regarded as coherent wave trains emitted by randomly distributed electrons. This may explain why the calculated Fano factor for this electron state in Eqn. (2.78) is equal to that of chaotic light.

2.3.2.2 Comparison to existing literatures

Banacloche [22] showed that the radiation is chaotic during the linear gain regime of the high-gain FEL starting from the noise, if the electrons are initially in momentum eigenstates prior to the FEL interaction. In his analysis, he attributed the random phase distribution of the initial electrons to the infinite width of the wave function in the position space, and found the same Fano factor as that for the chaotic light, Eqn. (2.78). Interestingly, this result is the same as what was just derived for electrons initially described by the minimum noise state.

Scully, Becker, and Zubairy [23] also investigated photon statistics in the linear gain regime of the FEL starting from the vacuum, using the one-electron nonreletivistic Bambini-Renieri Hamiltonian in the electron's comoving frame. Using the initial electron state of momentum eigenstate, the photon statistics was shown to be sub-Poissonian only if the gain is less than one. This does not contradict what we found from Eqn. (2.73).

Gjaja and Bhattacharjee [24] studied whether amplitude-squeezed light can be generated, in the linear gain regime of a FEL starting from the noise. They found that in a high-gain FEL, regardless of the initial state of the electrons, amplitude-squeezed light cannot be emitted. For a low-gain FEL, if the electrons are not entangled initially, and the initial wave functions of all electrons have the same width in position space and also in momentum space, they found that the amplitude-squeezed light cannot be emitted either. However, they discovered that some initially entangled state of the electrons can result in the amplitude-squeezed light, which is interestingly not accompanied by the sub-Poissonian photon statistics according to Eqn. (2.73).

The steady state FEL photon statistics is calculated to be super-Poissonian in the classical regime ($q \ll 1$), under the assumption of small gain per pass [25]. And the photon statistics of other conventional lasers is not sub-Poissonian [19].

2.3.3 Coherent spontaneous harmonic radiation (CSHR)

2.3.3.1 Classical CSHR driven by the fundamental mode

For the CSHR, we can obtain the approximate classical field equation in the linear gain regime. Contents of Section 2.3.3.1 are from a similar study for the 3rd harmonic field in Ref. [10].

For the high-gain FEL, the time evolution of the system in the 1-D theory is governed by the following equations:

$$\begin{aligned}
&\frac{d\theta_j}{d\hat{z}} = \hat{\eta}_j \\
&\frac{d\hat{\eta}_j}{d\hat{z}} = a_1 e^{i\theta_j} + a_3 e^{3i\theta_j} + \cdots + a_h e^{hi\theta_j} + c.c. \\
&\frac{da_h}{d\hat{z}} = -b_h \\
&b_h \equiv \langle e^{-hi\theta_j} \rangle \\
&\frac{da_h}{d\hat{z}} = -\frac{[\mathrm{JJ}]_h^2}{[\mathrm{JJ}]_1^2} \langle e^{-hi\theta_j} \rangle,
\end{aligned} \tag{2.88}$$

where h is the harmonic number. Here, we treat the bunching b_h perturbatively, which means that $|b_h| \sim O(\epsilon^h)$ and $a_h \sim O(\epsilon^h)$ with $\epsilon \ll 1$.

Dropping the higher order terms $\sim O(\epsilon^{h+1})$, we can obtain the differential equation for a_h as the following:

$$\begin{aligned}
&\frac{d^3 a_h}{d\hat{z}^3} = -\frac{[\mathrm{JJ}]_h^2}{[\mathrm{JJ}]_1^2} \frac{d^2 b_h}{d\hat{z}^2} = hi \frac{[\mathrm{JJ}]_h^2}{[\mathrm{JJ}]_1^2} \frac{d}{d\hat{z}} \langle e^{-hi\theta_j} \hat{\eta}_j \rangle \simeq hi \frac{[\mathrm{JJ}]_h^2}{[\mathrm{JJ}]_1^2} \langle e^{-hi\theta_j} \frac{d\hat{\eta}_j}{d\hat{z}} \rangle \\
&\simeq hi \frac{[\mathrm{JJ}]_h^2}{[\mathrm{JJ}]_1^2} (a_1 b_{h-1} + a_3 b_{h-3} + \cdots + a_h).
\end{aligned} \tag{2.89}$$

From Eqn. (2.89), we can obtain the following differential equation for a_1:

$$\frac{d^3 a_1}{d\hat{z}^3} = -\frac{d^2 b_1}{d\hat{z}^2} = \frac{d}{d\hat{z}} i \langle e^{-i\theta_j} \hat{\eta}_j \rangle \simeq i \langle e^{-i\theta_j} \frac{d\hat{\eta}_j}{d\hat{z}} \rangle \simeq i a_1. \tag{2.90}$$

The corresponding solution becomes the following, assuming that the FEL is a high-gain machine and that the exponentially-growing solution dominates:

$$a_1(\hat{z}) = A e^{-i\mu_{00}\hat{z}}, \tag{2.91}$$

where $\mu_{00} = \frac{-1+\sqrt{3}i}{2}$. Then, we need to obtain the expression for b_2. From Eqn. (2.88), we can obtain the following:

$$\begin{aligned}
&\frac{d^2 b_2}{d\hat{z}^2} \simeq -2i \langle e^{-2i\theta_j} \frac{d\hat{\eta}_j}{d\hat{z}} \rangle \simeq -2i a_1 b_1 = i \frac{d}{d\hat{z}} a_1^2, \\
&\therefore \frac{db_2}{d\hat{z}} = i a_1^2 \\
&\therefore b_2 = -\frac{1}{2\mu_{00}} a_1^2
\end{aligned} \tag{2.92}$$

Then, for a_3, the following can be obtained:

$$\frac{d^3 a_3}{d\hat{z}^3} = -\frac{[\mathrm{JJ}]_3^2}{[\mathrm{JJ}]_1^2} \frac{d^2 b_3}{d\hat{z}^2} = 3i \frac{[\mathrm{JJ}]_3^2}{[\mathrm{JJ}]_1^2} \frac{d}{d\hat{z}} \langle e^{-3i\theta_j} \hat{\eta}_j \rangle \simeq 3i \frac{[\mathrm{JJ}]_3^2}{[\mathrm{JJ}]_1^2} \langle e^{-3i\theta_j} \frac{d\hat{\eta}_j}{d\hat{z}} \rangle \simeq 3i \frac{[\mathrm{JJ}]_3^2}{[\mathrm{JJ}]_1^2} (a_3 + a_1 b_2). \tag{2.93}$$

Then from Eqs. (2.92) and (2.93), we can obtain the following:

$$\frac{d^3 a_3}{d\hat{z}^3} \simeq 3i\frac{[\mathrm{JJ}]_3^2}{[\mathrm{JJ}]_1^2}(a_3 - \frac{1}{2\mu_{00}}a_1^3). \tag{2.94}$$

We assume that the higher harmonic modes are driven by the fundamental mode (CSHR). Then we can obtain the following for a_3:

$$a_3(\hat{z}) \simeq -\frac{1}{18\mu_{00}}\frac{[\mathrm{JJ}]_3^2}{[\mathrm{JJ}]_1^2}a_1^3(\hat{z}) + a_3(0). \tag{2.95}$$

For b_3, we obtain the following equation:

$$\frac{d^2 b_3}{d\hat{z}^2} \simeq -3i\langle e^{-3i\theta_j}\frac{d\hat{\eta}_j}{d\hat{z}}\rangle \simeq -3i(a_1 b_2 + a_3) \simeq \frac{3i}{2\mu_{00}}\Big(1 + \frac{1}{9}\frac{[\mathrm{JJ}]_3^2}{[\mathrm{JJ}]_1^2}\Big)a_1^3(\hat{z}) - 3ia_3(0). \tag{2.96}$$

In Eqn. (2.96), $a_3(0)$ may not be that larger than $\frac{[\mathrm{JJ}]_3^2}{[\mathrm{JJ}]_1^2}a_1^3(\hat{z})$. Therefore, approximately, we can obtain the following expression for b_3:

$$\therefore\ b_3 \simeq \frac{1}{6i}a_1^3(\hat{z}), \tag{2.97}$$

which means that the harmonic bunching is mainly driven by the fundamental mode. Similarly, from Eqs. (2.95) and (2.97), we can deduce the following relations:

$$\begin{aligned} b_h &\propto a_1^h, \\ a_h &\propto a_1^h. \end{aligned} \tag{2.98}$$

Then, from Eqn. (2.89) we can obtain the following:

$$a_h(\hat{z}) = a_h(0) + k_h(\hat{z})a_1^h(0). \tag{2.99}$$

Then, promoting the classical field to the corresponding quantum operator, and ignoring the cavity loss, we can find that the hth harmonic field's quantum operator after the $(n+1)$th cavity round-trip can be related to that of the nth cavity round-trip as the following:

$$\mathfrak{a}_{h,n+1} = \mathfrak{a}_{h,n} + k_h\mathfrak{a}_{1,n}^h. \tag{2.100}$$

2.3.3.2 Photon statistics of CSHR

If we consider the cavity loss for the hth harmonic mode using the beam splitter model, we can obtain the following equations for the field operator, although it does not preserve the commutation relation ($[\mathfrak{a}_{h_1,n}, \mathfrak{a}_{h_2,n}^\dagger] = \delta_{h_1,h_2}$ does not infer $[\mathfrak{a}_{h_1,n+1}, \mathfrak{a}_{h_2,n+1}^\dagger] = \delta_{h_1,h_2}$):

$$\mathfrak{a}_{h,n+1} = \sqrt{\eta_h}e^{i\phi_{h,n}}\mathfrak{a}_{h,n} + \sqrt{1-\eta_h}e^{i\phi_{h,u,n}}\mathfrak{a}_{h,u,n} + k_h\mathfrak{a}_{1,n}^h. \tag{2.101}$$

Therefore, $\mathfrak{a}_{h,n}$ becomes the following:

$$\mathfrak{a}_{h,n} = \sqrt{\eta_h}^{n-1}e^{i\Phi_{h,1}}\mathfrak{a}_{h,1} + \sum_{j=1}^{n-1}\sqrt{\eta_h}^{n-j-1}e^{i\Phi_{h,j+1}}\left(k_h\mathfrak{a}_{1,j}^h + \sqrt{1-\eta_h}e^{i\phi_{h,u,j}}\mathfrak{a}_{h,u,j}\right), \tag{2.102}$$

where, as before, $\Phi_{h,j} = \sum_{k=j}^{n-1} \phi_{h,k}$. Consequently, the first two moments of the photon statistics become:

$$\langle \mathfrak{n}_h \rangle_n = |k_h|^2 \sum_{j,k=1}^{n-1} \sqrt{\eta_h}^{2(n-1)-(j+k)} \langle \mathfrak{a}'^{\dagger h}_{h,n_j} \mathfrak{a}'^{h}_{h,n_k} \rangle, \tag{2.103}$$

$$\langle \mathfrak{n}_h^2 \rangle_n = \langle \mathfrak{n}_h \rangle_n + \sum_{j,k,l,m=1}^{n-1} \sqrt{\eta_h}^{4(n-1)-(j+k+l+m)} |k_h|^4 \left\langle \mathfrak{a}'^{\dagger h}_{h,n_j} \mathfrak{a}'^{h}_{h,n_k} \mathfrak{a}'^{\dagger h}_{h,n_l} \mathfrak{a}'^{h}_{h,n_m} \right\rangle, \tag{2.104}$$

where $\mathfrak{a}'_{h,n_j} \equiv \mathfrak{a}_{1,j} e^{i\Phi_{h,j+1}/h}$.

In a similar way to what we did before, the Fano factor of the harmonic mode after the nth cavity round-trip, $F_{h,n}$, satisfies

$$F_{h,n} = \frac{\langle (\delta \mathfrak{C}_{h,n})^2 \rangle}{\langle \mathfrak{n}_h \rangle_n} + 1 \geq 1, \tag{2.105}$$

and the photon statistics is not sub-Poissonian for any initial state of the electrons. The Hermitian operator $\mathfrak{C}_{h,n}$ is:

$$\mathfrak{C}_{h,n} = |k_h|^2 \sum_{j,k=1}^{n-1} \sqrt{\eta_h}^{2(n-1)-(j+k)} \mathfrak{a}'^{\dagger h}_{h,n_j} \mathfrak{a}'^{h}_{h,n_k}. \tag{2.106}$$

2.4 Summary

According to the standard FEL theory, it does not seem possible that the photon statistics measured in Chen-Madey experiemnt can be sub-Poissonian, within the quantum CSHR model used in the above analysis.

The radiation in FEL is a non-linear phenomenon in principle [the motion of electrons is affected by all harmonic fields as can be seen from Eqn. (2.88), and the system of equations of motion for a, b, and P of Eqn. (1.6) is not closed in general]. Then, considering the non-linearity used to generate sub-Poissonian light which can be seen from the squeeze operator [26], one could doubt the possible sub-Poissonian light generation within the FEL. However, in contrast to the non-linearity corresponding to the squeeze operator, for a frequency mode of the radiation field for the FEL in the classical regime, the ratio of the number of photons that would break the condition of Eqn. (2.2) (originating from higher frequency photons' split into that mode's photons) to the number of total photons of that mode (including the photons which many lower frequency photons coalesce into) would be insignificant. This might explain why the non-linearity in the classical FEL does not accompany the sub-Poissonian light, which could be verified more rigorously by a future study.

Chapter 3

Observed Fano factor of FEL light

In this chapter, the layout and result of Chen-Madey experiment in Refs. [3] and [13] are summarized. The contents of this chapter (except Section 3.1.5) are from Refs. [3] and [13].

As the theoretical study of the FEL photon statistics can be more easily done at the fundamental mode compared to the CSHR as shown in Chapter 2, one would prefer to perform a FEL photon count at the fundamental mode. However, the PMT's quantum efficiency at the fundamental mode of MARK III FEL ($2.68\mu m$) is close to zero and the observed Fano factor may converge to one despite the actual Fano factor at the source, according to Eqn. (2.44). Therefore, Chen and Madey measured the photon statistics of the 7th CSHR ($382nm$) where comparably high quantum efficiency (25%) of PMT is available. As explained in Section 2.3.3.1, the 7th CSHR is produced by the nonlinear components of the wiggle motion in the undulator.

3.1 Experimental layout

3.1.1 Operation parameter

3.1.1.1 Optical beam characteristics

MARK III FEL is made of a linearly polarized undulator composed of an array of permanent magnets. The radiation wavelength of the fundamental mode is $2.68\mu m$, and that of the 7th CSHR is $382nm$. The undulator deflection parameter K is 1.1349. The optical cavity is $2.046m$ long with $53.23cm$ Rayleigh range for the fundamental mode. The characteristics of the optical beam and MARK III FEL operation parameters are presented in Tables 3.1 and 3.2.

Optical beam parameters	**Value**
λ_1	$2.68\mu m$
λ_7	$382nm$
Cavity round-trip time	$13.66ns$

Table 3.1: Optical beam profile [13].

MARK III FEL Parameters	**Value**
Undulator period	$2.3cm$
Number of undulator periods	47
Undulator strength parameter (K)	1.13
Rayleigh range	$53.23cm$
Cavity loss at λ_1	14%
Cavity loss at λ_7	32.3%
Transmission at λ_1	5.5%
Transmission at λ_7	25%

Table 3.2: MARK III FEL operation parameters [13].

3.1.1.2 Electron beam characteristics

The electron gun and the linac of MARK III FEL are both powered by the 30MW Klystron at 2.856GHz RF. The continuous wave RF source of the Klystron is pulsed through a PIN diode triggered at 15Hz, and the spacing between two adjacent electron micropulses are about 350ps. The electron beam energy is well stablized from micropulse to micropulse with 0.4% Full Width Half Maximum (FWHM) spread within an individual macropulse. The characteristics for the electron beam are provided in Table 3.3, and the micropulse and macropulse are described in Fig. 3.1.

Electron beam parameters	**Value**
Macropulse length	2μs
Macropulse repetition rate	15Hz
Micropulse length	2ps
Micropulse repetition rate	2.856GHz
Average beam energy	43.5MeV
Energy spread (FWHM)	0.4%
Peak micropulse current	30A
Average micropulse current	171.4mA

Table 3.3: Electron beam profile [13].

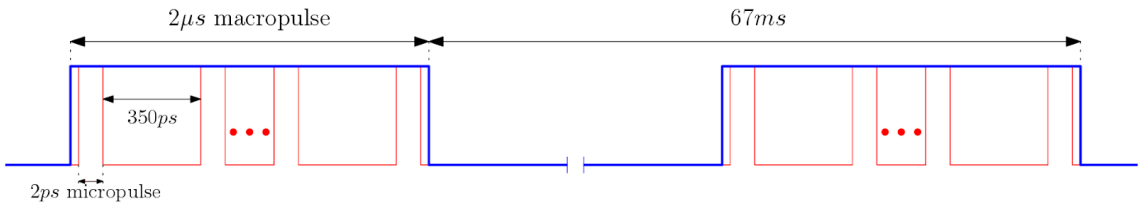

Figure 3.1: Micropulse and macropulse [13].

3.1.2 Diagram of the experiment

3.1.2.1 Set-up of the experiment

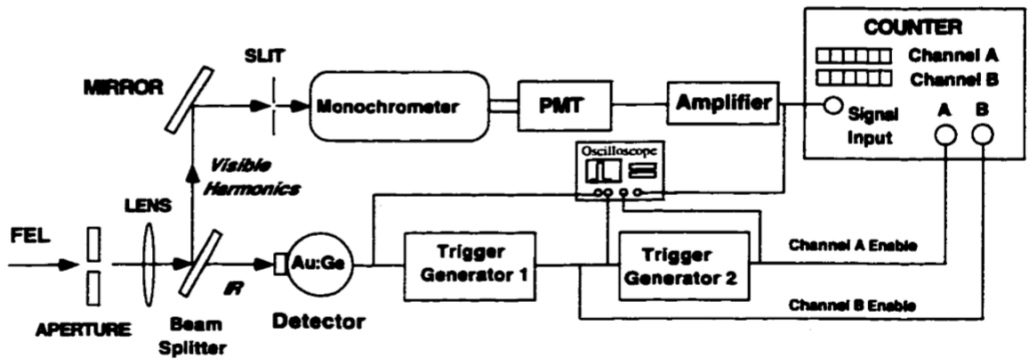

Figure 3.2: Set-up of the experiment [3].

The set-up of Chen-Madey experiment is shown in Fig. 3.2. The output FEL light from the cavity passes through an aperture and then a lens before it reaches a dichroic beam splitter that transmits the fundamental mode and reflects the CSHR. The beam line for the CSHR consists of a monochrometer, an adjustable slit, a fast, high quantum efficiency PMT, and an amplifier. The CSHR is brought to a focus at the adjustable slit and monochromator combination; the former is used to adjust the count rate, while the latter selects the 7th CSHR. Since the slit is at the focal plane of the lens, its size defines the effective optical mode waist of the measured 7th harmonic mode.

Measurements of the 7th CSHR are triggered by the signal of the IR fundamental which is measured by a fast Au:Ge IR detector (monitored by a 1 GHz oscilloscope). A start signal is sent to the counter by trigger generator 1 when the amplitude of the IR detector reaches a pre-set voltage (Fig. 3.3), followed by an end signal after $80ns$. During the $80ns$ observation window the counter records the number of 7th CSHR pulses from the PMT along channel B. In addition, trigger generator 2 enables channel A of the counter to record the number of background photons, as shown in Fig. 3.4. The background photons are observed to be absent.

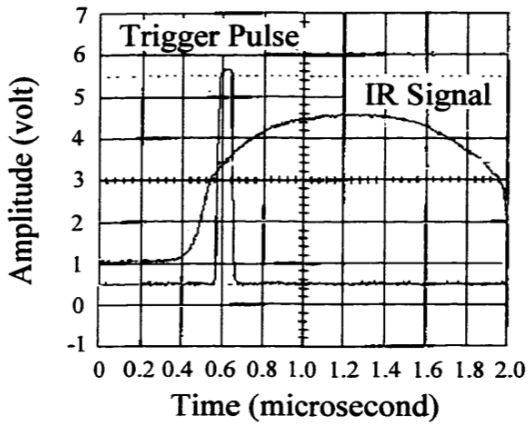

Figure 3.3: The observation window of the data [13].

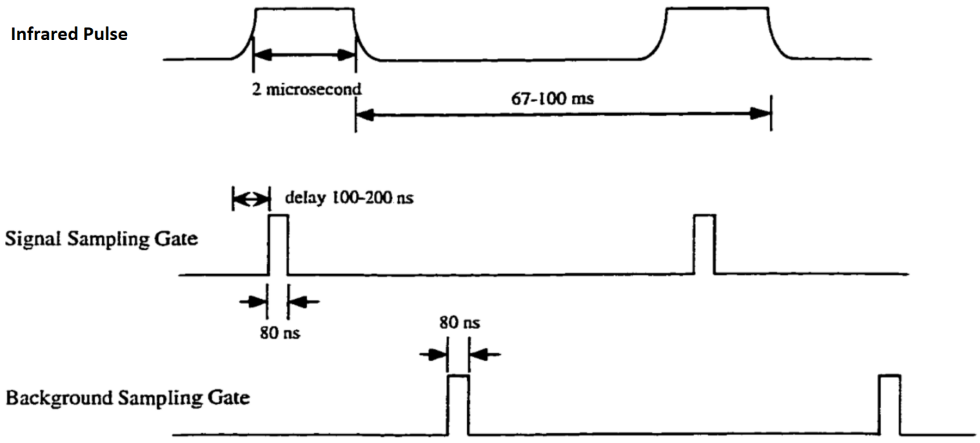

Figure 3.4: The timing relation of the infrared pulse and the observation windows [13].

The linac delivers about 230 electron micropulses within each $80ns$ observation window which corresponds to about 6 cavity round-trip times. There are on average 19.5 radiation micropulses at the fundamental circulating in the cavity while the macropulse is on. Emission into the 7th CSHR is low, and on average the PMT measures ≤ 3 photons during any single $80ns$ observation window.

Because the PMT pulse's height is much lower than the counter's normal operation voltage (1V), the PMT pulses are amplified by the amplifier before being fed into the counter. Thus amplified PMT pulses are registered by the counter. The counter has a built-in discriminator that sets the threshold, and pulses with amplitude lower than the one produced by a single photon which is experimentally determined is rejected.

The goal of the measurement is the Fano factor F of the counted photon numbers.

3.1.3 Reduction of the classical fluctuations in the photon count

To measure the quantum fluctuations of photon statistics accurately, according to Eqn. (2.21), it is important to eliminate the wholly classical fluctuations of the photon statistics. Therefore, Chen and Madey examined whether the classical fluctuations exist and claimed that they are absent in Chen-Madey experiment.

As MARK III FEL is a linac-driven FEL, insuring uniform conditions within the system's linac driver could be feasible. As the electron pulses are not reused, wake field instability would be diminished; the electron distribution near the RF cavity is determined by the electron gun and thus reproducible.

The intensity of the counted 7th CSHR is dictated by the modulation of the electron beams which is almost solely influenced by the intensity of the fundamental mode. Therefore, the generation of the 7th CSHR across many ensemble may be uniform, as the $80ns$ observation window is initiated when the fundamental mode intensity reaches a pre-set value while the average current of the electron beam is also stablized during the experiment. To guarantee uniform IR pulse level and shape in the 80ns observation window, the stability of the FEL gain is checked and it is verified.

From Fig. 3.3, it can be seen that the fundamental mode's voltage corresponding

to the start of the observation window is already under the effect of IR detector's saturation. Therefore, an exponential fitting of the intensity is done within a time period which does not overlap with the IR detector's saturation regime or observation window (red dots in Fig. 3.5). The gain of the fundamental mode over a single pass which is obtained from the fit is consistent with the calculation obtained from Eqn. (2.64); $|g(\hat{L}_u)|^2 \simeq 1.56$, which is well consistent with the gain observed, considering the 14% cavity loss. From the fitting, the fundamental mode's voltage corresponding to the start of the observation window is found to be approximately $4.4V$. And the saturation power of fundamental mode, which can be estimated by using an attenuator that enables the amplitude to be away from the IR detector's saturation regime, is observed to be at least $340V$. This means that the observation window starts when the voltage is less than approximately 1.3% of the FEL saturation level. Hence, the observation window is at the linear gain regime which is away from the saturation. Therefore, the chaotic intensity fluctuations due to the side band instability can be eliminated in the observation window.

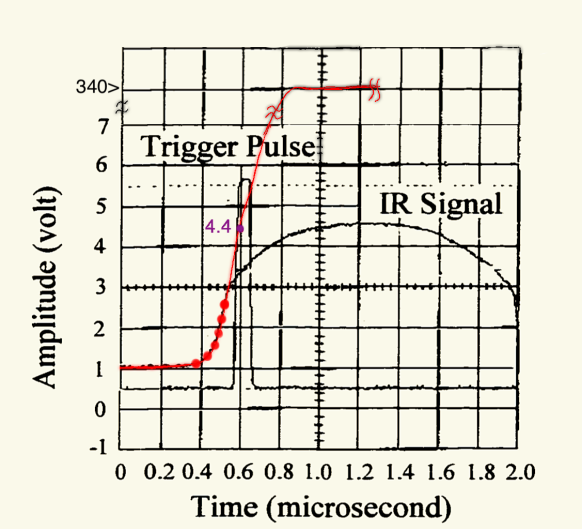

Figure 3.5: Exponential fit for the data of fundamental mode's intensity, prior to the detector's saturation (edited from Ref. [13]).

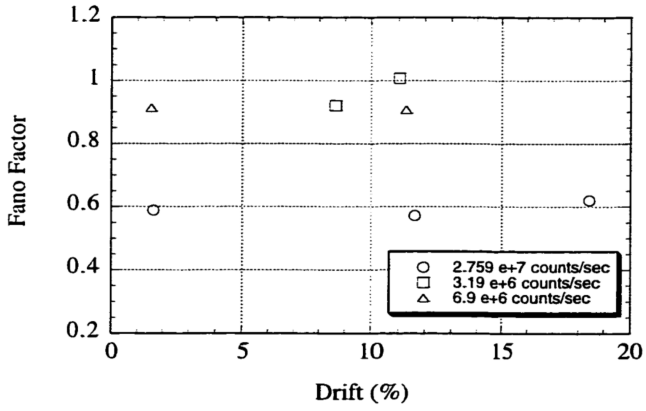

Figure 3.6: Effect of optial system's drift on the Fano factor [13].

Regarding the possible long-period (time scales of seconds or minutes) classical fluctuations due to the drift of mirrors, slits, etc., in the optical transport system, drifts in the count rate due to the angular drift of the laser beam are observed. The data sets with more than 20% drifts in the count rate are disposed; among the data from sets of ensembles, any set of which count rate differs more than 20% from the mean of sets is discarded. The effect of drift on the Fano factor is studied by checking if the set with larger drifts has different Fano factor compared to set of smaller drift. As shown in Fig. 3.6, a correlation between Fano factor and the drift is not found. Consequently the classical fluctuations from the drift might be verified to be diminished.

Based on the above considerations, Chen and Madey concluded that the wholly classical fluctuations of these bunches is diminished to the extent that each group of 230 micropulses in the $80ns$ observation window can be considered as the indistinguishable members of an ensemble.

3.1.4 Optical system of the photon count

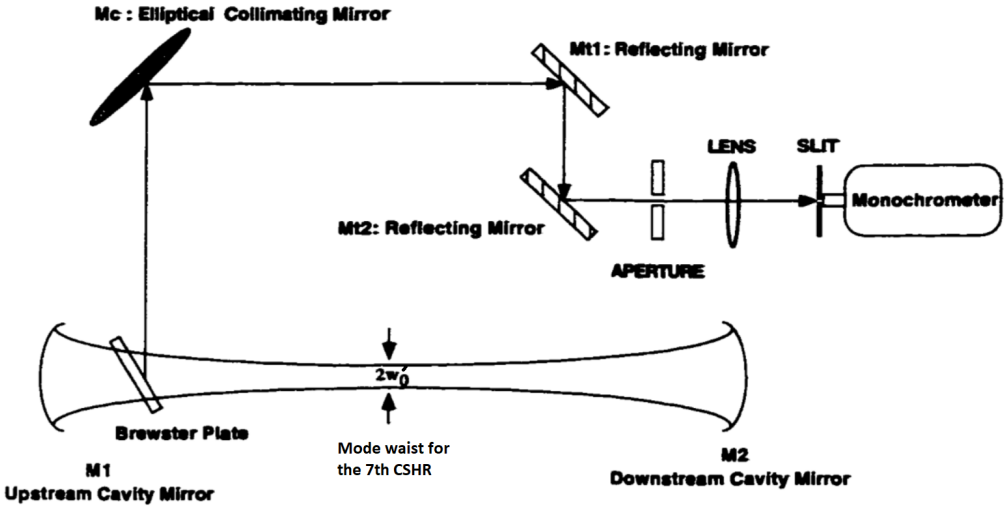

Figure 3.7: Diagram of the optical system for the 7th CSHR [13].

The optical system of Fig. 3.2 is detailed in Fig. 3.7, and the parameters of the optical components are listed in Table 3.4. The radius of curvature of cavity mirrors and the cavity length are such that the configuration matches the lowest Gauss-Laguerre mode at the fundamental mode of which mode waist at the center.

The 7th CSHR's mode waist size w_0' is determined by the slit size, r_s. The relationship between them can be obtained from the transfer matrix from the cavity to the entrance of the monochrometer. We set the waist of the constructed mode to be at the distance z_0 from the down stream mirror as shown in Fig. 3.8.

Parameter	Definition	Value(m)
R_1	Radius of curvature for upstream cavity mirror M1	1.3
f_1	Focal length for upstream cavity mirror	0.65
R_2	Radius of curvature for downstream cavity mirror M2	1.3
f_2	Focal length for downstream cavity mirror	0.65
L_c	Cavity length	2.046
R_c	Radius of curvature for collimating mirror Mc	11.31
f_c	Focal length of collimating mirror	5.655
d_1	Distance between M1 and Mc	6.2093
f	Focal length of the lens in front of slit	0.2
d_2	Distance between Mc and the focal lens	36.6486
r_s	Beam spot size at slit	$\sim 3 \times 10^{-5}$
d_3	Distance between focal length and slit	0.2

Table 3.4: MARK III FEL optical system's specification [13].

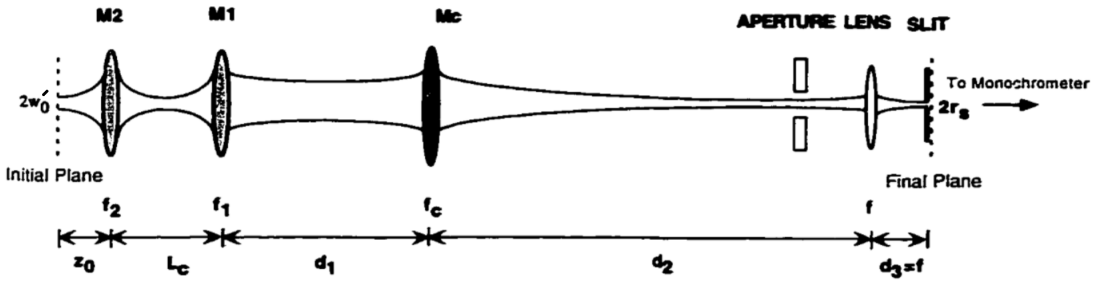

Figure 3.8: Equivalent 7th CSHR's optical transport system [13].

The complex beam parameter q_f of Gaussian beam at the final plane is related to the value q_i of Gaussian beam at the initial plane, according to the following formula:

$$\frac{1}{q_f} = \frac{C + D(1/q_i)}{A + B(1/q_i)}, \tag{3.1}$$

where A, B, C, and D are the elements of the transfer matrix from the initial plane to the final plane:

$$M = \begin{pmatrix} A & B \\ C & D \end{pmatrix}. \tag{3.2}$$

Recall that the matrix for a focusing lens with focal length f is:

$$M_L = \begin{pmatrix} 1 & 0 \\ -\frac{1}{f} & 1 \end{pmatrix}. \tag{3.3}$$

And for a free drift with distance d, it is:

$$M_d = \begin{pmatrix} 1 & d \\ 0 & 1 \end{pmatrix}. \tag{3.4}$$

Let M_{int} be the matrix corresponding to the transport system inside the cavity:

$$M_{int} = \begin{pmatrix} 1 & 0 \\ -\frac{1}{f_1} & 1 \end{pmatrix} \begin{pmatrix} 1 & L_c \\ 0 & 1 \end{pmatrix} \begin{pmatrix} 1 & 0 \\ -\frac{1}{f_2} & 1 \end{pmatrix} \begin{pmatrix} 1 & z_0 \\ 0 & 1 \end{pmatrix}, \tag{3.5}$$

and let M_{ext} be the one outside the cavity:

$$M_{ext} = \begin{pmatrix} 1 & d_3 \\ 0 & 1 \end{pmatrix} \begin{pmatrix} 1 & 0 \\ -\frac{1}{f_L} & 1 \end{pmatrix} \begin{pmatrix} 1 & d_2 \\ 0 & 1 \end{pmatrix} \begin{pmatrix} 1 & 0 \\ -\frac{1}{f_c} & 1 \end{pmatrix} \begin{pmatrix} 1 & d_1 \\ 0 & 1 \end{pmatrix}. \tag{3.6}$$

Then the matrix corresponding to the transformation from the initial plane to the final plane becomes the following:

$$M = M_{ext} M_{int} = \begin{pmatrix} A & B \\ C & D \end{pmatrix}, \tag{3.7}$$

where the elements are functions of z_0. In general, the complex beam parameter q can be linked to optical parameters as the following:

$$\frac{1}{q(z)} = \frac{1}{R(z)} - i\frac{\lambda}{\pi w(z)^2}, \tag{3.8}$$

where $w(z)$ is the radiation beam size, $R(z)$ is the radius of curvature of the radiation wave front, and λ is the wavelength of the radiation beam. As the radiation beam is at the waist at both initial and final planes R is infinite at these planes, and thus we can obtain the following for q_i and q_f:

$$\begin{aligned} \frac{1}{q_i} &= -i\frac{\lambda_7}{\pi w_0'^2}, \\ \frac{1}{q_f} &= -i\frac{\lambda_7}{\pi r_s^2}. \end{aligned} \tag{3.9}$$

Here, we assume that r_s is small enough to ensure that at the final plane R can be approximated to be infinite. For the given $1/q_f$, according to Eqn. (3.1), there is only one z_0 yielding zero real component of $1/q_i$, which is the solution. Then, using Eqs. (3.1) and (3.9), w_0' also can be obtained. Then, the Rayleigh range z_R of the constructed 7th CSHR's lowest transverse mode can be obtained from the following:

$$z_R = \frac{k_7 w_0'^2}{2}. \tag{3.10}$$

In Chen-Madey experiment, r_s is around $30\mu m$, w_0' is around $50\mu m$, and z_R is around $2cm$, which means that the mode expands fast.

The adjustable slit serves as a mode filter; the slit width dictates the waist size of the optical mode into which the $7th$ harmonic photons are emitted. Then, as the number of electrons that contribute for the emission to that mode is proportional to the cross section of the mode waist, the number of photons emitted into that mode can be altered by the slit width. Hence, changing the slit openings can differ the photon intensity arriving at the PMT so that various count rates can be achieved. In this way, the photon statistics at different count rates are measured. The range of the slit openings is designed to avoid the PMT's saturation, to ensure the operation in the single-photon condition; such a low count rate of the 7th CSHR is satisfied

without using an attenuator. The single-photon condition is vital to measure the photon statistics accurately.

If the slit size becomes so small that the optical volume of the mode exceeds the cavity volume, the radiation is attenuated. Both attenuated and unattenuated datum are measured.

3.1.5 Dead time of the counter

3.1.5.1 Definition

The dead time is the recovery time during which the counter does not react to any photoelectron pulses [27]. Considering the 200MHz bandwidth of the counter's discriminator, the dead time for Chen-Madey experiment may be close to the pulse width of $8ns$ (using the clipping technique, the width of PMT pulse corresponding to an incident photon has been reduced to approximately $8ns$ from $15ns$, as shown in Fig. 3.9) [13].

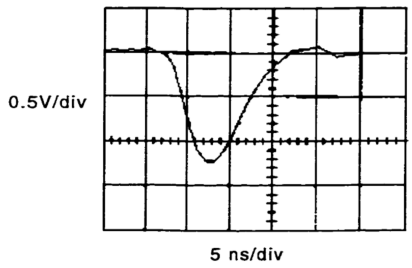

Figure 3.9: PMT pulse for a photon; FWHM of approximately $8ns$ [13].

The following contents of Section 3.1.5.1 are from Ref. [27]. The dead time effect becomes more significant as the count rate increases. Therefore, if any counting measurement's count rate is so high that one cannot ignore the dead time effect, the dead time effect should be considered. Two commonly used models of the dead time effect are *paralyzable* and *non-paralyzable* response models. The basics of the two models are illustrated in Fig. 3.10.

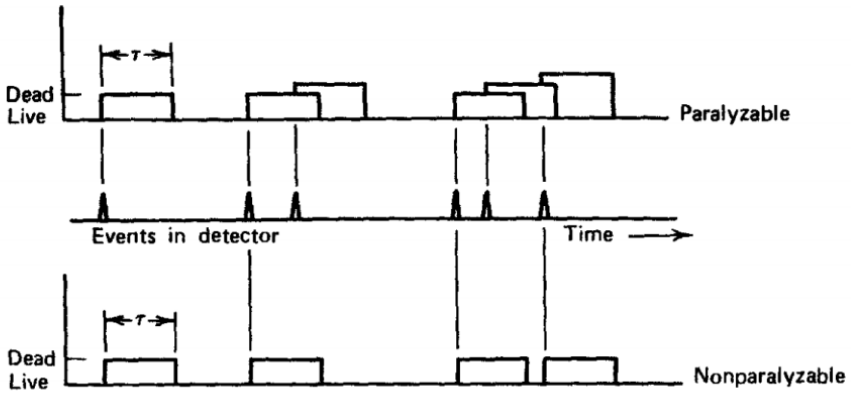

Figure 3.10: Illustration of two models of dead time for the counter [27].

These models mimic idealized dead time phenomenon. At the center line of Fig. 3.10, six pulses reaching the counter are illustrated. At the bottom line of Fig. 3.10, the model of dead time is assumed to be non-paralyzable. In this model, a fixed dead time τ is assumed to follow each true pulse during the "live period" of the detector. Any signal pulses that arrive during the dead period are lost and assumed not to affect whatsover on the behavior of the counter. In the example shown in the figure, the non-paralyzable detector records four pulses out of the six true pulses. In contrast, the behavior of paralyzalbe counter is shown at the top line of Fig. 3.10. The same dead time τ is assumed to follow each true pulse during the live period of the counter. Pulses arriving during the dead period are not recorded, and extend the dead time by another unit following the lost pulse. In the example of Fig. 3.10, only three pulses are recorded out of the six true pulses.

The two models predict the same first-order losses. Therefore, for small count rate, the difference between two models diminish. However, for high count rate, the loss of the paralyzable model becomes more significant. The two models are in some sense two extremes of idealized behavior, and real counting systems will often exhibits a behavior between these two extremes.

We may quantitatively examine the response of a detecting system to a steady-state source composed of input pulses. We assume that the counting time (T) is long enough to regard n (true interaction rate) and m (recorded count rate) as average rates. Our goal here is to obtain an expression for n as a function of m and dead time (τ). In the non-paralyzable case, the total amount of time when the detector is dead is $mT\tau$. As n and m are regarded as average rates, $m\tau$ can be considered to be average fraction of all time when the detector is dead. Therefore, $n \times (m\tau T)$ is the number of lost event. Therefore, we can obtain the following:

$$(n - m)T = nm\tau T. \tag{3.11}$$

Solving for n, we obtain

$$n = \frac{m}{1 - m\tau}. \tag{3.12}$$

In the paralyzable case, m is the rate of occurrences of time intervals between true events which exceed τ. Assuming that the input signal is a Poisson source, the probability that the no events occur during $(0, t)$ and the first event occurs during $(t, t + dt)$ is the following:

$$ne^{-nt}dt. \tag{3.13}$$

Therefore, the probability that two adjacent true events' time interval is larger than τ can be obtained by integrating Eqn. (3.13) between τ and ∞:

$$\int_{\tau}^{\infty} ne^{-nt}dt = e^{-n\tau}. \tag{3.14}$$

The rate of occurrence of such intervals is then obtained by multiplying Eqn. (3.14) by the true rate n, which results in the following:

$$m = ne^{-n\tau}. \tag{3.15}$$

For low rates ($n \ll \frac{1}{\tau}$) both Eqs. (3.12) and (3.15) dictate the following:

$$m \simeq n(1 - n\tau). \tag{3.16}$$

3.1.5.2 Photon clustering, dead time, and observed photon statistics

If there is photon clustering within the observation window, it results in an additional reduction of measured Fano factor below that of Poisson source with a constant emission rate as shown in Fig. 3.11, which in turn would suppress F beyond that predicted from dead time alone [28]. This can be explained as the followings. For bunched light, photons appear as cluster compared to an un-bunched light. As a result, the dead time effect would result in smaller Fano factors for such bunched light than for an un-bunched light; if the photons are completely bunched the counted number is always one and the variance is zero (zero Fano factor). Hence, for a photon counting experiment, one must check whether the photon clustering affects the measurement.

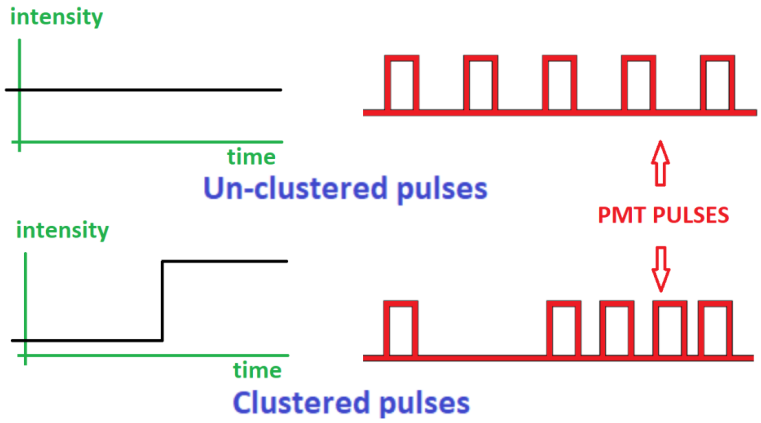

Figure 3.11: Photon clustering.

3.2 Experimental result

3.2.1 LED reference light

In Chen-Madey experiment, to investigate both the dead time and the reliability of the counting system, some series of measurements using a known Poisson light source is conducted, and compared to the result with the theoretical curve (using non-paralyzable dead time model) for the dead-time-modified un-clustered Poisson radiation (DTMPR). A red light emitting diode (LED) is selected as the Poisson source [for this LED, even if $F_{in} \neq 1$, due to the low PMT's quantum efficiency less than 0.5%, $F_{out} \simeq 1$, according to Eqn. (2.44)]. In the low count rate, the dead time effect becomes negligible and the true photon statistics of the LED can be readily identified. In such low count rate, a series of measurement verifies Fano factor of unity, and the differential and integral probability distribution matched the theoretical ones of the Poisson distribution. Therefore, the LED can be considered as a reliable Poisson source.

3.2.1.1 Correlation analysis of the PMT voltage

To investigate the photon clustering, a correlation analysis of the PMT voltage explained below is used. As the PMT response is not fast enough to distinguish the adjacent micropulses apart by $350ps$ as shown in Fig. 3.9, such analysis may not be

sufficient to rigorously study the photon clustering occurring in adjacent micropulses. However, the analysis may provide some information of the photon clustering occurring over long time (at the order of cavity round-trip time).

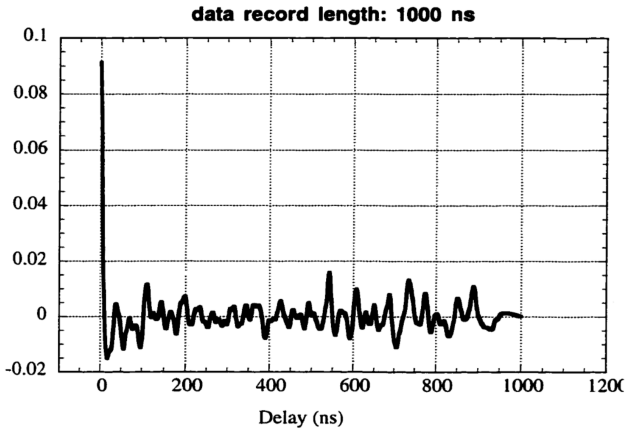

Figure 3.12: Normalized auto-correlation function for the reference LED at count rate 3.0×10^7 counts/sec [13].

If $V(t)$ is the PMT voltage, the normalized auto-correlation function at time delay τ can be defined as the following:

$$G(\tau) \equiv \frac{1}{T} \int_0^{t_{max}} V(t)V(t+\tau)dt, \tag{3.17}$$

where t_{max} is the record length. The total length of time, $T = t_{max} + \tau_{max}$, is in the order of one macropulse. For convenience, $G(\tau)$ is calculated using the adjusted amplitude $V^*(t)$, instead of using $V(t)$. The $V^*(t)$ is related to $V(t)$ by

$$V^*(t) = V(t) - V_{dc}, \tag{3.18}$$

where

$$\int_0^{t_{max}} \{V(t) - V_{dc}\}dt = 0. \tag{3.19}$$

The advantage of using $V^*(t)$ is that the dc component of the signal is suppressed because the average value of $V^*(t)$ is zero.

Although there should be significant loss of information of the auto-correlation function due to the finite length of the data record, the auto-correlation function can be accurate if the time scale of τ is much shorter than t_{max}. As shown from the auto-correlation function of PMT voltage in Fig. 3.12, there is no indication of photon clustering for the LED source.

3.2.1.2 Photon statistics of the LED source

The photon number of LED source is counted at comparable count rates as those for the measured 7th CSHR. The pulses are $3\mu s$ long with repetition frequency of 15Hz, which mimics the electron micropulse of MARK III FEL. The two trigger generators create two gate pulses that enable the two recording channels on the counter. The first trigger has the counter count photon numbers when the LED is on, whereas the second

trigger has the counter record the background counts when the LED is off (background photons are absent). The timing of these pulses are shown in Fig. 3.13. The trigger gate is located during a time period when the LED pulse exhibits a uniform intensity.

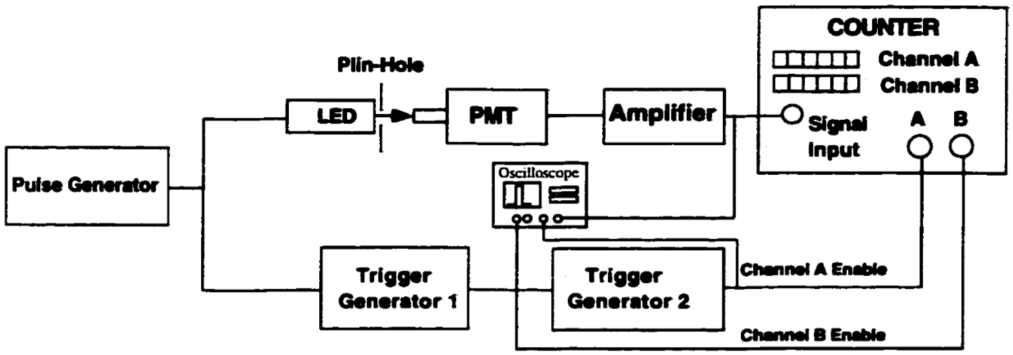

Figure 3.13: Diagram of the photon counting experiment of the LED [13].

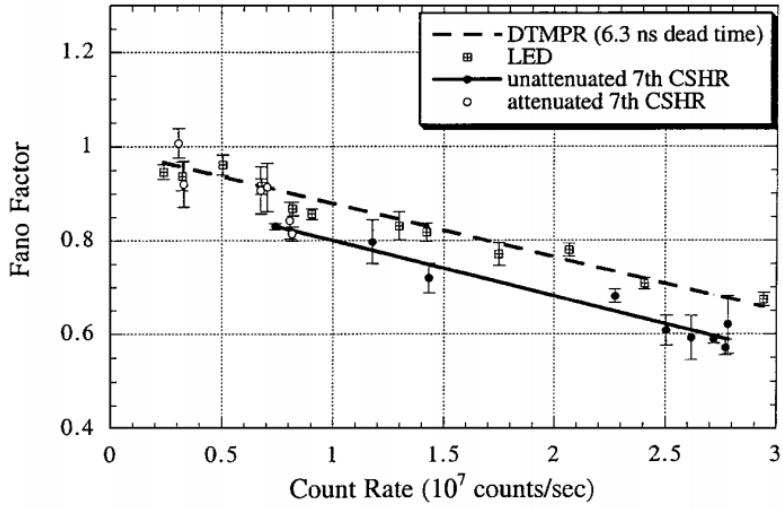

Figure 3.14: Observed reduction of the Fano factor for the 7th CSHR (solid line) compared to the theoretical DTMPR curve (dashed line) and an experimental Poisson source (LED) (the error bars indicate the measured standard deviation of the experimental data points) [3].

The count rates in the LED experiment are altered by the size of a pinhole located in front of the LED and by neutral density filter. As the count rate increases Fano factor is observed to decrease due to the dead time effect.

3.2.1.3 Equivalent PMT's response to the LED and the 7th CSHR

The PMT's response to the LED and the 7th CSHR are verified to be equivalent, which is shown in Figs. 3.15 and 3.16. In both cases, the threshold of discriminator of the counter is 1V. The shape and height of the PMT pulses for both cases are

similar. And the PMT pulse's height is consistent with that produced by a single photon emission which is observed in the low intensity LED experiment.

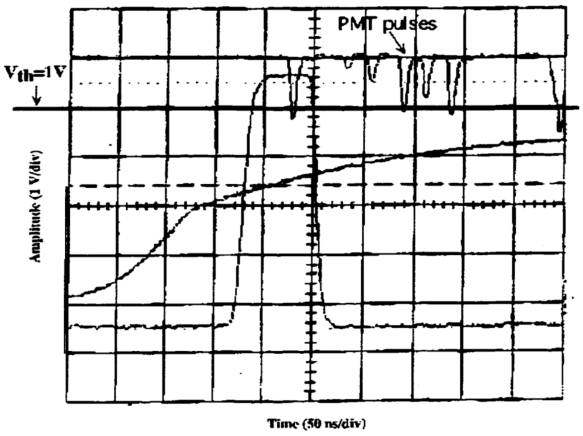

Figure 3.15: PMT pulses of the 7th CSHR [13].

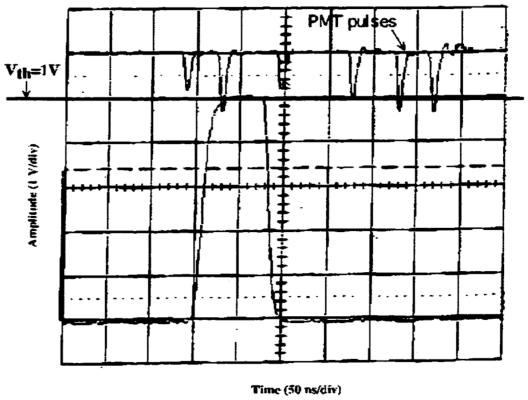

Figure 3.16: PMT pulses of the LED [13].

3.2.2 Reduced Fano factor of the 7th CSHR

As mentioned in Section 3.1.4, various count rates are achieved by adjusting the width of the slit in front of the monochrometer. The LED and 7th CSHR data are plotted together with the theoretical DTMPR (dead-time-modified un-clustered Poisson radiation) curve in Fig. 3.14.

The DTMPR curve in Fig. 3.14 seems to be a reasonable fit to the LED data with a 1% χ^2 confidence level (C.L.), assuming a dead time of 6.3 ns. Although the unattenuated 7th CSHR data cannot be fit by the DTMPR curve because of an extremely low χ^2 C.L. (less than 10^{-4}), it can be fit by a straight line offset from the DTMPR curve. The χ^2 C.L. for this ad hoc fit is quite high (25%). This cannot be due to statistical errors in the data; the 7th CSHR differs from the DTMPR curve by more than 3 standard deviations at a count rate of 7.5×10^6 counts/s, and more than 6 standard deviations at 2.75×10^7 counts/s. Considering the quantum efficiency of 12%, Chen and Madey concluded that the actual Fano factor for the 7th CSHR is no more than about 0.243 at the source, using the offset and Eqn. (2.44).

Chapter 4

The experimental photon clustering study

As mentioned in Section 3.1.5, the dead time is known to reduce Fano factor more effectively for bunched light. The photon clustering may occur in the photon counting of Chen-Madey experiment if the emission probability of the CSHR increases due to FEL gain. Therefore, it is important to investigate whether any photon clustering affected the measurement, before identifying the Fano factor at the source. After some studies, Chen and Madey argued that there is no photon clustering in the observation window [3, 13]. Then they compared the observed Fano factor and DTMPR curve assuming no photon clustering, and concluded that the observed reduction of Fano factor represents an observation of sub-Poisson light, as shown in Chapter 3.1.4. In this chapter, their argument of no photon clustering in the observation window in Refs. [3] and [13] is re-examined.

4.1 Photon clustering over observation window

They dismissed some mechanisms that may lead to photon clustering within the observation window: 1) clustering in adjacent electron micropulses, 2) multiple photons emitted by the same electron micropulse, 3) correlation in photon pulses associated with stored optical energy in the cavity, and 4) chaotic photon clustering.

4.1.1 Clustering in adjacent electron micropulses

For the 1) clustering in adjacent electron micropulses which results in a cluster of photons spaced too closely to be resolved by the PMT, they claimed that the times of emission of electrons are both deterministic and non-overlapping as determined by the precise, periodic bunched structure of the electron beam, and thus the photon emissions from adjacent electron micropulses are statistically independent. This argument seems to be reasonable.

4.1.2 Multiple photons emitted by the same electron micropulse

For the mechanism 2) multiple photons emitted by the same electron micropulse, they claimed that the observed PMT pulses are essentially all of the same height at all count rates inside the observation window. However, this qualitative description may not

rigorously inform us of whether there is a photon clustering. Nevertheless, indeed their claim may be true because of the following reason: even at the maximum count rate measured, as the average number of the photons emitted by an electron micropulse is much less than 0.1 the possibility that one micropulse emits more than one photon can be dismissed.

4.1.3 Correlation in micropulses due to optical energy stored in the cavity

As Chen and Madey did for the LED source study (Section 3.2.1.1), they obtained the auto-correlation function of the PMT traces of the 7th CSHR to investigate the possibility of clustering due to stored optical energy in the cavity, over $257.5ns$ from the start of observation window. They assumed that the clustering may accompany the enhancement of the auto-correlation function at the cavity round-trip time (13.7 ns), and they found that the PMT auto-correlation function displayed a small local minimum at this time interval as shown in Fig. 4.1. Therefore, they claimed that such photon clustering can be ruled out. However, within the $80ns$ observation window, there are at most only about three $8ns$ wide pulses. Therefore, the auto-correlation function obtained from one observation window (the pmt pulses of Fig. 3.11) cannot faithfully reflect the classical intensity profile (intensity of Fig. 3.11). We are therefore, unable to see how Chen and Madey could exclude the possibility of photon clustering based on their investigation.

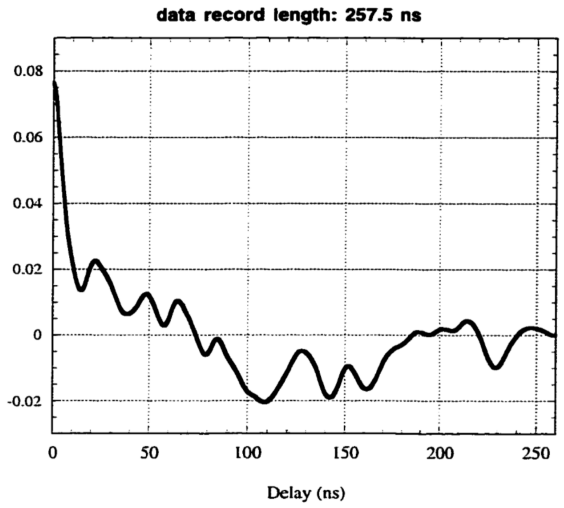

Figure 4.1: Normalized auto-correlation function for the 7th CSHR at count rate of 2.97×10^7 counts/sec [13].

4.1.4 Chaotic clustering

Chen and Madey studied possible photon clustering due to the chaotic nature of the 7th CSHR. However, in the study they assumed that the coherence time (t_{coh}) of the 7th CSHR is much longer than the dead time ($\sim 6ns$), which is not the case for MARK III FEL: t_{coh} is near the micropulse length [13]. And even if t_{coh} is very longer than the micropulse length as they kept only the first two lowest order terms in terms of

unmodified count mean for the variance calculation, their calculation of Fano factor for dead-time-modified chaotic light in Fig. 4.3 is off from the true value in Ref. [28]. In short, their study is irrelevant to the photon clustering of the 7th CSHR.

4.1.5 A study of clustered LED sample

Chen and Madey happened to come across a LED source exhibiting strong photon clustering (auto-correlation function exceeding 30% at the first maxima with a period of $50ns$ and a coherence time of $400ns$) as shown in Fig. 4.2.

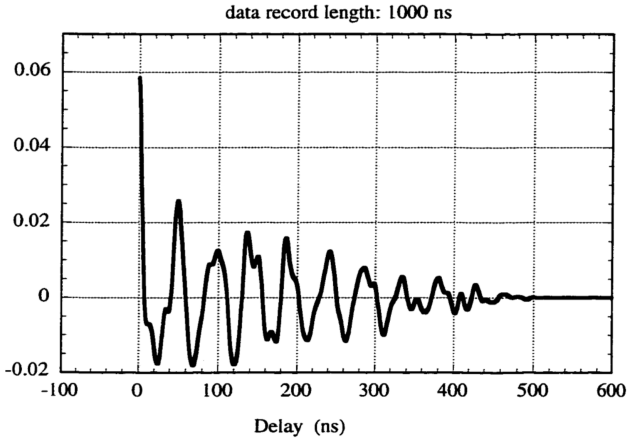

Figure 4.2: Normalized auto-correlation function for the clustered LED source at count rate of 2.95×10^7 counts/sec [13].

They argued that while the Fano factor for the clustered LED is reduced relative to DTMPR curve, the reduction is small compared to that observed for the 7th CSHR, which is shown in Fig. 4.3. Hence, they argued that the reduction of 7th CSHR data does not originate from the photon clustering. However, the clustered LED source of Fig. 4.2 is just one example of many types of photon clustering. Ruling out one example cannot guarantee that there was no photon clustering.

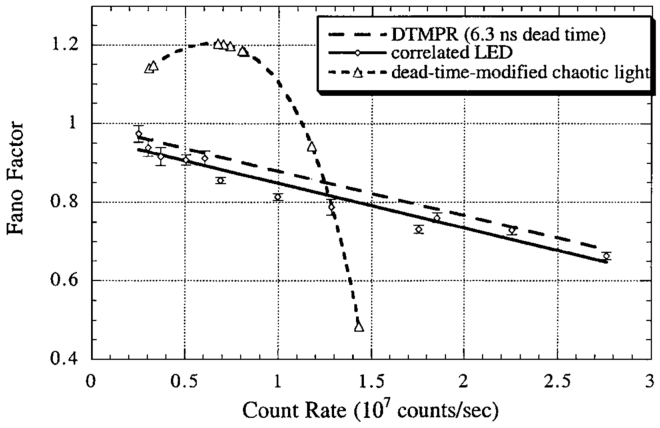

Figure 4.3: Dependence of the Fano factor on the count rate for chaotic light and for light source with strong photon clustering [3].

Chapter 5

Simulated photon statistics

As we found in Chapter 4, the possibility that the photons are clustered within the observation window of Chen-Madey experiment cannot be ruled out based on their photon clustering study. Since Mark III FEL is no longer available to repeat the experiment, we have simulated Chen-Madey experiment.

The steps of the simulation are:

1. Determine the FEL power in the fundamental and the 7th CSHR as a function of the cavity round-trip number.

2. Determine the starting time (cavity round-trip number) of the $80ns$ observation window by using the experimentally measured ratio of the power in the fundamental at the start of observation window to that in saturation.

3. Determine the 7th CSHR power during the $80ns$ window determined in step 2 to set the emission probability, and simulate the measurement including dead time.

5.1 Negligible chaotic nature of the 7th CSHR

As shown in Eqn. (2.105), the 7th CSHR in the observation window could possess some chaotic nature. The coherence time of the 7th CSHR is near the micropulse length as mentioned in Section 4.1.4. And the emitted photon number by a micropulse is a lot less than 0.1. Then from Eqs. (2.32) and (2.33), chaotic nature of the 7th CSHR is negligible. Hence, in the observation window we assume that the 7th CSHR is a Poisson source.

5.2 The 7th CSHR's intensity profile

5.2.1 Introduction to GINGER

To simulate the intensity of the 7th CSHR as a function of time, GINGER code [29] is used. The following contents of Section 5.2.1 are from Ref. [29]. GINGER is a multidimensional simulation code, which was first developed in mid-1980's and has since been improved. For the electromagnetic field, it is based on angular symmetry in the transverse plane and thus the coordinates are $r - z - t$, which increases the

computation speed, although the simulated intensity of spontaneous emission can be inaccurate. For the charged particles, it is not based on such simplification and thus the coordinates are $x - y - z - t$. GINGER is polychromatic simulation code, which means that all field quantities and particle bunchings can vary at multiple frequencies. Therefore, it can incorporate the effects of shot noise, slippage, current and energy variation, and side band growth.

5.2.2 Time of observation window

The simulation's input parameters are in accordance with the experiment, which is shown in Table 5.1 (the specification of MARK III FEL can be obtained from Refs. [3], [13], [30], and [31]), and the simulated intensity profile for the fundamental mode stored in the cavity is shown in Fig. 5.1. From Fig. 3.5, the intensity ratio of the oscillator saturation to the start of observation window is approximately 0.01. Using this ratio, we can determine the cavity round-trip number corresponding to the start of the observation window, from the simulated intensity. As shown in Fig. 5.1, this is determined to be 58.

The observed and simulated intensity of the fundamental mode (the voltage of IR detector) are fitted using a exponential line (the red dots of Fig. 3.5 for the data, and the blue dots of Fig. 5.1 for the simulation) in Fig. 5.2. The two lines' gains are approximately the same.

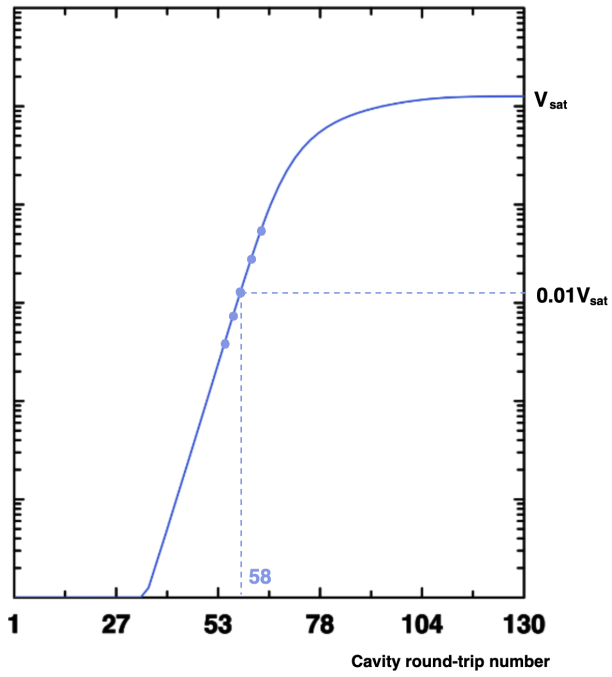

Figure 5.1: Simulated intensity of the fundamental mode (vertical axis is log scale).

The simulated intensity profile for the higher harmonics is given in Fig. 5.3. The intensity curve of the 7th CSHR cannot be fit well using an exponential line, whereas it can be fit better with a linear line as shown in Fig. 5.4.

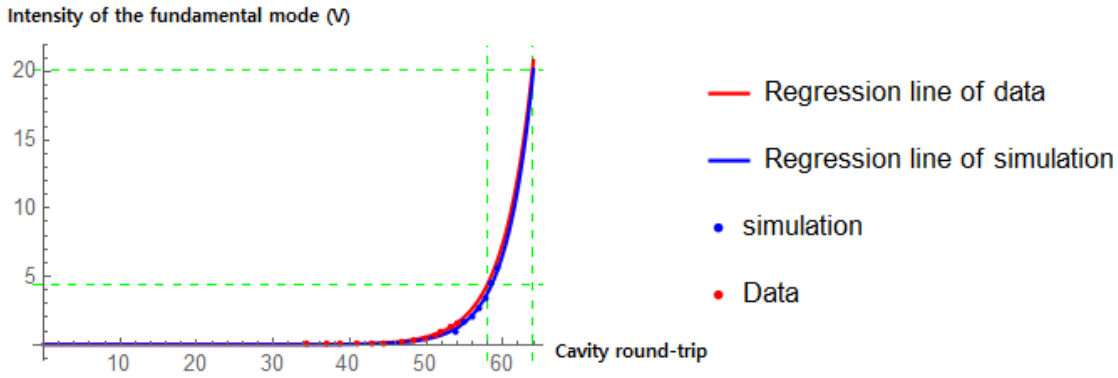

Figure 5.2: Simulated and experimentally observed intensity of the fundamental mode.

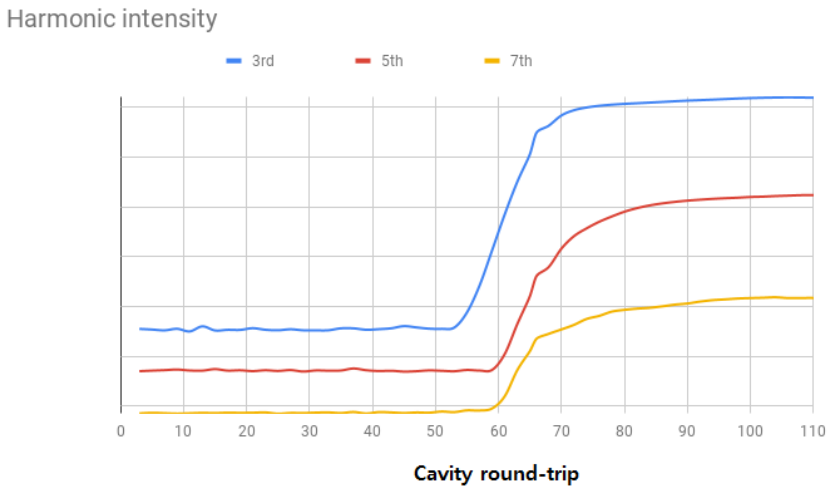

Figure 5.3: Simulated intensity of the harmonic modes (vertical axis is log scale).

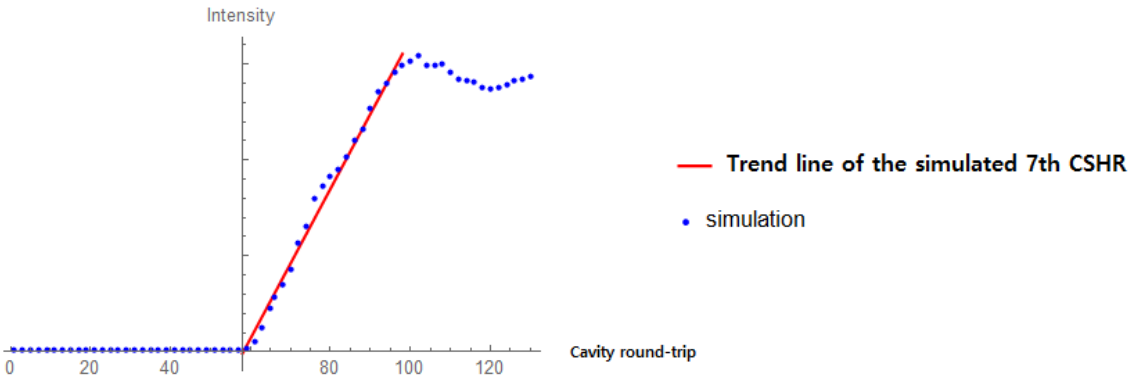

Figure 5.4: The simulated 7th CSHR's intensity (vertical axis is linear scale).

Simulation parameters	Value	Unit
I	30	A
γ	86.127	
$\delta\gamma$ (Gaussian distribution)	0.146	
ϵ_x^n (x-axis normalized electron emittance)	8×10^{-6}	$mm \cdot mrad$
ϵ_y^n (y-axis normalized electron emittance)	4×10^{-6}	$mm \cdot mrad$
w_x (x-axis electron beam's RMS size at the waist)	1.91×10^{-4}	m
w_y (y-axis electron beam's RMS size at the waist)	1.35×10^{-4}	m
$\beta_x \equiv \frac{\langle x^2 \rangle}{\epsilon_x}$ (at the undulator entrance)	1.06	m
$\beta_y \equiv \frac{\langle y^2 \rangle}{\epsilon_y}$ (at the undulator entrance)	0.39	m
$\alpha_x \equiv -\frac{\langle xx' \rangle}{\epsilon_x}$ (at the undulator entrance)	1	
$\alpha_y \equiv -\frac{\langle yy' \rangle}{\epsilon_y}$ (at the undulator entrance)	0	
Pulse length	2	ps
Number of photon beam slices	192[a]	
Number of electron beam slices	100	
Electrons' number per slice	30496	
λ_1	2.68	μm
ρ	3.826×10^{-3}	
w_0 (fundamental mode's waist size)	6.73×10^{-4}	m
w_0' (7th CSHR's waist size)	4.9×10^{-5}	m
Rayleigh length	0.531	m
λ_u	0.023	m
B_0	0.53	T
Cavity detuning	0.05[b]	Slippage length
Pulse window length	3.84	ps
Total number of cavity round-trip	130	
Cavity length	2.05[c]	m
R_1	1.3	m
R_2	1.3	m
Round-trip cavity loss at the fundamental mode[d]	14%	

Table 5.1: Simulation's input parameters.

[a] The slice-averaging time is guaranteed to be much less than the coherence time.
[b] Although several features of the supermode theory complicate its application in this situation [30], according to Ref. [32] the value yielding the maximum FEL gain is approximately 0.2. However, the saturated fundamental mode's power is maximized at about 0.05, according to the simulation, while the gain of both fundamental mode and harmonic modes remains approximately the same for values between 0.05 and 0.2.
[c] The optical beam's waist is set to locate at the center of the cavity.
[d] The simulation does not store harmonic fields from the previous cavity round-trips, in the cavity.

MARK III FEL's 7th CSHR's intensity observed from another experiment [33] (at different FEL parameters) is shown in Fig. 5.5. This also indicates that the 7th CSHR's increasing intensity can be fit well by a linear line in the linear gain regime.

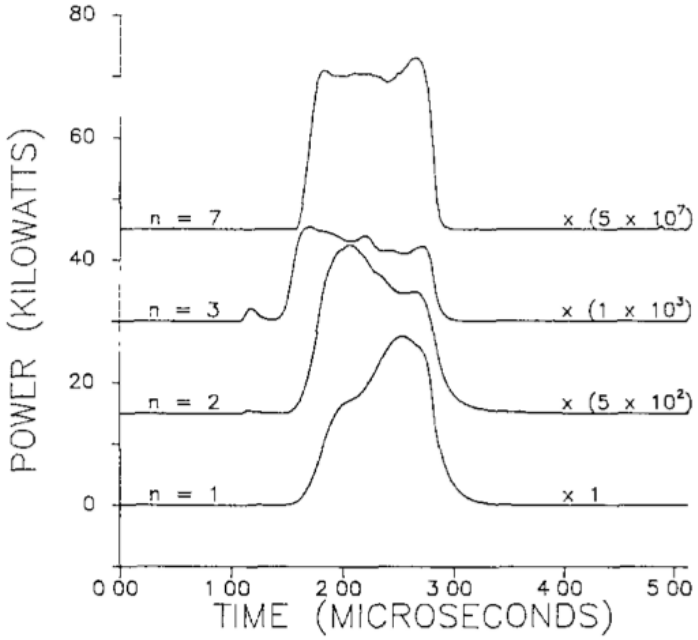

Figure 5.5: Observed 7th harmonic mode's intensity [33].

5.2.3 2-D approximation and spontaneous emission rate

As mentioned in Section 5.2.1, GINGER employs $r - z - t$ coordinates in describing radiation field, and thus trace only the angular symmetric portion of the field. However, as MARK III FEL electrons' motion need not be angular symmetric, the emitted spontaneous emission may not be angular symmetric either. Therefore, the simulated spontaneous emission rate corresponding to the symmetric mode can be smaller than the true rate of the full mode including the asymmetric modes [34], although difference between the symmetric mode and the full mode is diminished once the FEL leaves the spontaneous emission regime, due to the gain guiding [10]. As the intensity for the spontaneous emission regime affects the photon clustering over the observation window, the correct spontaneous emission intensity needs to be obtained in our simulation. Therefore, we will calculate the intensity difference between the symmetric (angular symmetric in the transverse plane) mode and the full mode, which will be used to adjust the GINGER's spontaneous emission intensity (the increase rate in the regime after the spontaneous emission regime ends is not adjusted).

The following contents of Section 5.2.3 are from Ref. [34]. The electric field created by the generic jth electron in the undulator is the following in the frequency domain (L_u is the length of undulator, $\mathbf{x}$ and $\mathbf{x}'$ are the transverse position and angular divergence, respectively. $\boldsymbol{\phi}$ is the transverse angle, and t_j is the electron's undulator entrance time):

$$\mathcal{E}_{\nu,j}(\boldsymbol{\phi}, \frac{L_u}{2}) = e^{ickt_j} e^{-ik\boldsymbol{\phi}\cdot\mathbf{x}_j} \mathcal{E}^0_{(\nu-2\eta_j)}(\boldsymbol{\phi} - \mathbf{x}'_j; \frac{L_u}{2}), \tag{5.1}$$

where the field created by the reference electron satisfying $(\mathbf{x}, \mathbf{x}') = (\mathbf{0}, \mathbf{0})$ and $(t_j, \gamma_j) = (0, \gamma_r)$ locating at the center of undulator is (the pre-factors are omitted):

$$\mathcal{E}^0_{(\nu-2\eta_j)}(\boldsymbol{\phi} - \mathbf{x}_j; \frac{L_u}{2}) = \int_0^{L_u} dz e^{i\frac{k}{2}(\boldsymbol{\phi}-\mathbf{x}'_j)^2(-\frac{L_u}{2}+z)(1-2\eta_j)} e^{i(\Delta\nu-2\eta_j)k_u z}. \tag{5.2}$$

Therefore, Eqn. (5.1) becomes

$$\mathcal{E}_{\nu,j}(\boldsymbol{\phi}, \frac{L_u}{2}) = e^{ickt_j} \int_{-\frac{L_u}{2}}^{\frac{L_u}{2}} e^{i[-k\boldsymbol{\phi}\cdot\mathbf{x}_j + k/2(\boldsymbol{\phi}-\mathbf{x}'_j)^2(1-2\eta_j)z]} e^{i(\Delta\nu-2\eta_j)k_u(z+\frac{L_u}{2})} dz. \tag{5.3}$$

And the second exponent can be simplified as the following, in the polar coordinate $[\boldsymbol{\phi} = (\rho, \psi)]$:

$$-k\boldsymbol{\phi}\cdot\mathbf{x}_j + k/2(\boldsymbol{\phi}-\mathbf{x}'_j)^2(1-2\eta_j)z = i\big[\frac{k}{2}(\phi^2 + {x'_j}^2)(1-2\eta_j)z + \rho k|\mathbf{x}_j + \mathbf{x}'_j(1-2\eta_j)z|\cos\alpha\big], \tag{5.4}$$

where α is:

$$\alpha \equiv \psi - \Theta(z), \tag{5.5}$$

and $\Theta(z)$ is the angle of $-\{\mathbf{x}_j + \mathbf{x}'_j(1-2\eta_j)z\}$. Then using Jacobi-Anger identity, Eqn. (5.3) can be expanded in series as:

$$\begin{aligned}\mathcal{E}_{\nu,j}(\boldsymbol{\phi}, \frac{L_u}{2}) = e^{ickt_j} \int_{-\frac{L_u}{2}}^{\frac{L_u}{2}} dz \sum_{n=-\infty}^{\infty} i^n J_n(\rho k|\mathbf{x}_j + \mathbf{x}'_j(1-2\eta_j)z|) e^{in\{\psi-\Theta(z)\}} \\ \times e^{i(\Delta\nu-2\eta_j)k_u(z+\frac{L_u}{2})} e^{i\frac{k}{2}(\phi^2+x'^2_j)(1-2\eta_j)z}.\end{aligned} \tag{5.6}$$

The angular symmetric mode is only the $n = 0$ term of the expansion, and it becomes:

$$\mathcal{E}^s_{\nu,j}(\boldsymbol{\phi}, \frac{L_u}{2}) = e^{ickt_j} \int_{-\frac{L_u}{2}}^{\frac{L_u}{2}} dz J_0(\rho k|\mathbf{x}_j + \mathbf{x}'_j(1-2\eta_j)z|) e^{i(\Delta\nu-2\eta_j)k_u(z+\frac{L_u}{2})} e^{i\frac{k}{2}(\phi^2+x'^2_j)(1-2\eta_j)z}. \tag{5.7}$$

The flux is proportional to $|\mathcal{E}_{\nu,j}|^2$, and it becomes the following for the full mode:

$$\frac{d\mathcal{F}_j}{d\omega d\boldsymbol{\phi}} \propto |\mathcal{E}_{\nu,j}|^2 = \int_{-\frac{L_u}{2}}^{\frac{L_u}{2}} \int_{-\frac{L_u}{2}}^{\frac{L_u}{2}} e^{i\frac{k}{2}\rho^2(z-s)} dz ds = \frac{L_u^2}{2}\mathrm{sinc}^2(\frac{k\rho^2}{4}L_u), \tag{5.8}$$

and the following for the symmetric mode:

$$\frac{d\mathcal{F}^s_j}{d\omega d\boldsymbol{\phi}} \propto |\mathcal{E}^s_{\nu,j}|^2 = \int_{-\frac{L_u}{2}}^{\frac{L_u}{2}} \int_{-\frac{L_u}{2}}^{\frac{L_u}{2}} J_0^2(\rho k x_j) e^{i\frac{k}{2}\rho^2(z-s)} dz ds = \frac{L_u^2}{2}\mathrm{sinc}^2(\frac{k\rho^2}{4}L_u) J_0^2(\rho k x_j). \tag{5.9}$$

The flux from multiple electrons is

$$\mathcal{F} = \sum_j \mathcal{F}_j. \tag{5.10}$$

Assuming that the electrons do not have the angular divergence or energy spread, that the radiation has only the resonance frequency component ($\Delta\nu = 0$), and that the electrons are distributed in transverse plane in the form of $f(\mathbf{x}) = \frac{1}{\sigma_x^2} e^{-\frac{x^2}{2\sigma_x^2}}$, the flux becomes the following for the full mode:

$$\frac{d\mathcal{F}}{d\boldsymbol{\phi}} \propto \mathrm{sinc}^2(\frac{k\rho^2}{4}L_u), \tag{5.11}$$

and the following for the symmetric mode:

$$\frac{d\mathcal{F}^s}{d\boldsymbol{\phi}} \propto \mathrm{sinc}^2(\frac{k\rho^2}{4}L_u)\int_0^\infty xJ_0^2(\rho kx)\frac{1}{\sigma_x^2}e^{-\frac{x^2}{2\sigma_x^2}}dx = \mathrm{sinc}^2(\frac{k\rho^2}{4}L_u)e^{-k^2\rho^2\sigma_x^2}I_0(k^2\rho^2\sigma_x^2), \tag{5.12}$$

where $I_n(x)$ is the modified first kind of Bessel function. Therefore, the ratio of fluxes becomes:

$$\frac{\mathcal{F}^s}{\mathcal{F}} = \frac{\int_0^\infty \frac{d\mathcal{F}^s}{d\boldsymbol{\phi}}\phi d\phi}{\int_0^\infty \frac{d\mathcal{F}}{d\boldsymbol{\phi}}\phi d\phi}, \tag{5.13}$$

which becomes approximately 0.42 for the 7th CSHR of MARK III FEL ($\sigma_x \simeq 1.85 \times 10^{-4}m$ is used). So the 7th CSHR's spontaneous emission intensity simulated by GINGER is adjusted by dividing by 0.42, in our simulation.

5.3 Fano factor simulation

The last cavity round-trip number when the spontaneous emission dominates in the 7th CSHR may be 58, according to Fig. 5.3. And from the 58th cavity round-trip, the 7th CSHR intensity increases approximately in a linear manner. The simulated intensity of the 7th CSHR as a function of cavity round-trip number is presented in Fig. 5.6.

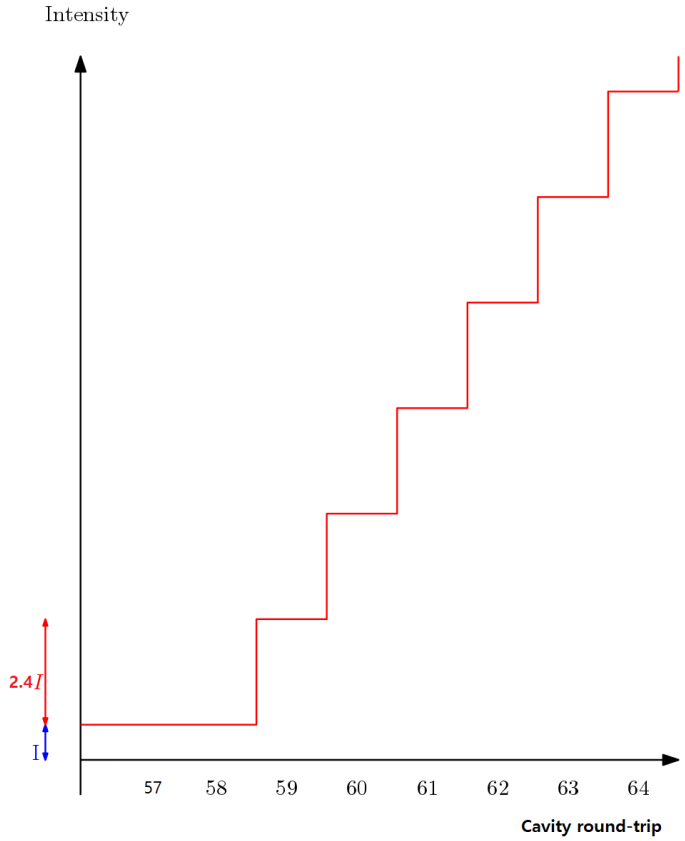

Figure 5.6: Simulated linearly increasing 7th CSHR intensity, which continues for about 30 cavity round-trips from the 58th cavity round-trip (vertical axis is linear scale).

Then using Mathematica's random Poisson source generator with intensity varying in time in accordance with the simulated one (Fig. 5.6), we simulate the photon emission. Then the photons are counted considering the two models of dead time (paralyzable and non-paralyzable). For the study of auto-correlation function of PMT voltages, PMT pulses are also simulated as shown in Fig. 5.7; whenever a photon emission is generated from the generator, a square pulse of width with $8ns$ is superposed onto the PMT traces. The photon count and the simulation of PMT pulses are done at various count rates.

Figure 5.7: PMT traces simulated by Mathematica.

5.3.1 Simulated Fano factor in consistent with the observation

If the observation window starts at the 58th cavity round-trip, the simulated Fano factor becomes the following (the data line is based on both the attenuated and unattenuated ones as the source is assumed to be Poissonian, the number of simulated ensembles is 4000, and the shaded region corresponds to 3σ band, for all the following simulated Fano factors in the dissertation):

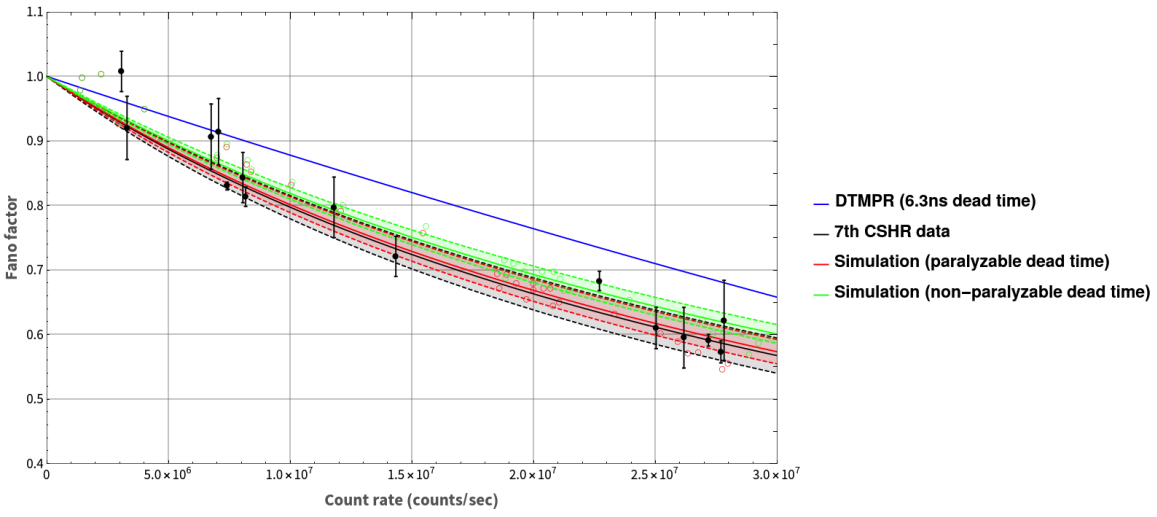

Figure 5.8: Simulated Fano factor, for the observation window starting at the 58th cavity round-trip.

As shown in Fig. 5.8, the paralyzable dead time model explains the data well, while the non-paralyzable model also explains almost well. The PMT voltage's simulated auto-correlation function over $257.5ns$ (from the start of the observation window) is given in Fig. 5.9 (it is averaged over 4000 ensembles, and dt: dead time, and T_0: cavity round-trip, for all the following simulated auto-correlation functions in the dissertation). It is in accordance with the observed one.

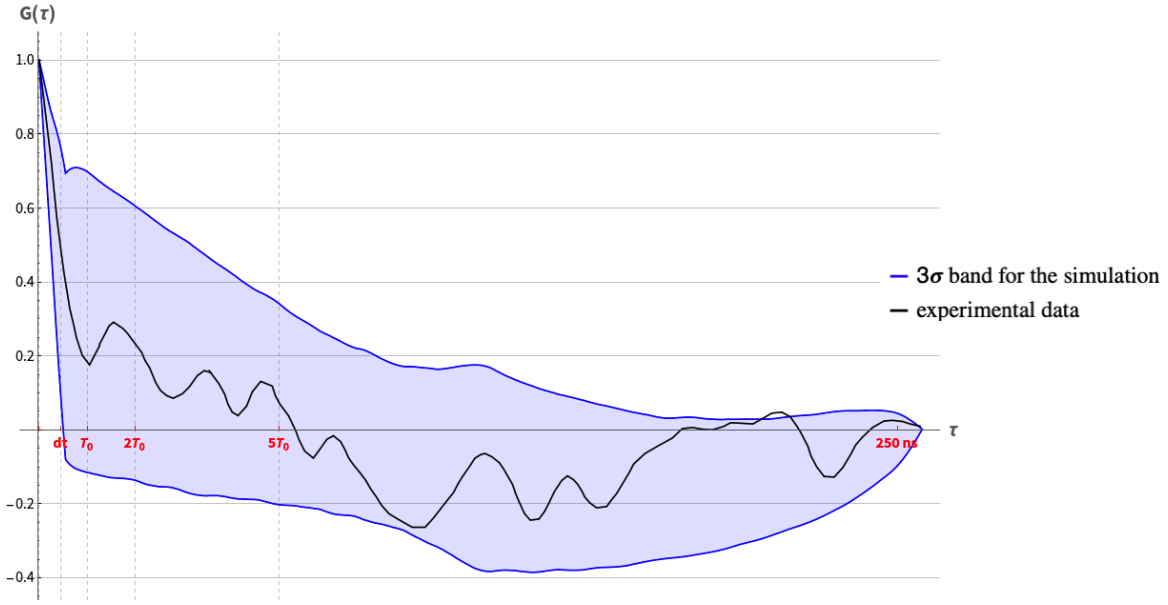

Figure 5.9: PMT voltage's auto-correlation function, for the observation window starting at the 58th cavity round-trip.

As can be seen from Fig. 5.9, the simulated auto-correlation function for the case when photon clustering exists within the observation window does not infer a local maximum at the cavity round-trip. This contradicts the argument of Chen and Madey in their photon clustering study (Section 4.1.3) which is used by them to claim no photon clustering in the observation window.

5.3.2 Observation window starting at other cavity round-trip numbers

There can be some uncertainties for the FEL parameters used in the simulation. Furthermore, only the lower limit of the oscillator saturation intensity of the fundamental mode, which is used to locate the observation window, is available. Consequently, the determined starting cavity round-trip number (58) for the observation window is somewhat uncertain. Therefore, some observation windows starting at other cavity round-trip numbers around 58 are chosen (as the band-pass of the monochrometer used in Chen-Madey experiment is not available, the location of observation window cannot be deduced from the count rate). Then the Fano factor and the auto-correlation function of the PMT voltages corresponding for other observation windows are checked whether they can be consistent with the experimentally observed ones, which is summarized in Table 5.2.

5.3.2.1 Observation window starting at the 59th cavity round-trip

If the observation window starts at the 59th cavity round-trip, the intensity ratio of the one at the end of the observation window to that at the beginning decreases significantly compared to that corresponding to observation window starting at the 58th cavity round-trip. Therefore, as can be seen from Fig. 5.10, the reduction of Fano factor is not large enough to explain the observed data, if the dead time is

Table 5.2: Possibility that the data can be explained by the standard FEL theory, depending on the starting cavity round-trip number of the observation window. NP: non-paralyzable dead time, P: paralyzable dead time. ◯: consistent, △: approximately consistent, ×: inconsistent.

Starting number	54		55		56		57		58	
Dead time type	NP	P	NP	P	NP	P	NP	P	NP	P
Fano factor	×	×	×	×	◯	◯	◯	◯	◯	◯
Auto-correlation	×		×		×		×		△	
Starting number	59		60		61		64			
Dead time type	NP	P	NP	P	NP	P	NP	P		
Fano factor	×	△	×	×	×	×	×	×		
Auto-correlation	◯		◯		◯		◯			

non-paralyzable (for the paralyzable dead time, the data may be consistent with the simulation).

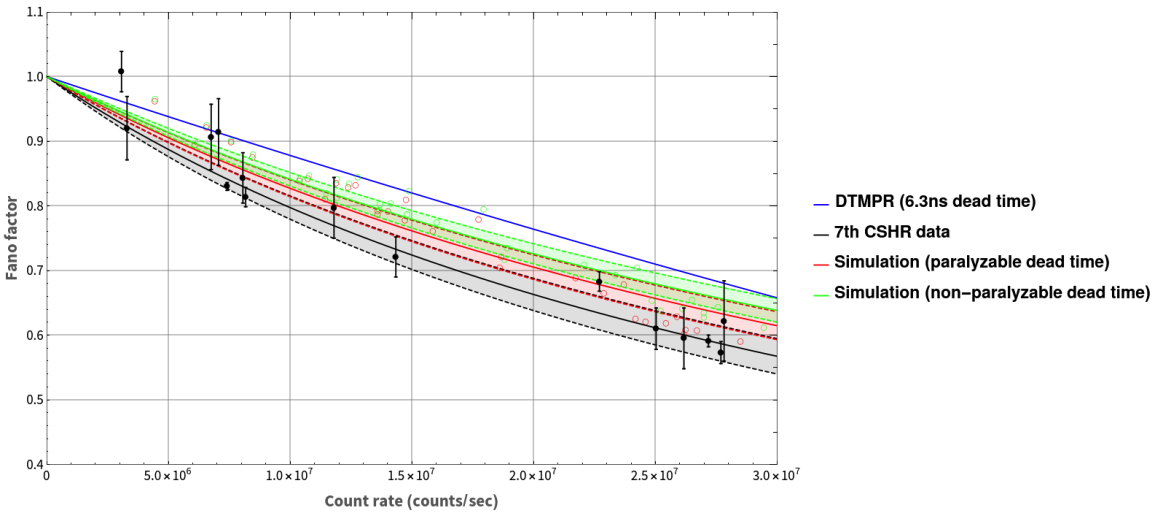

Figure 5.10: Simulated Fano factor, for the observation window starting at the 59th cavity round-trip.

On the other hand, the simulated auto-correlation function is still in accordance with the observed one as can be seen from Fig. 5.11.

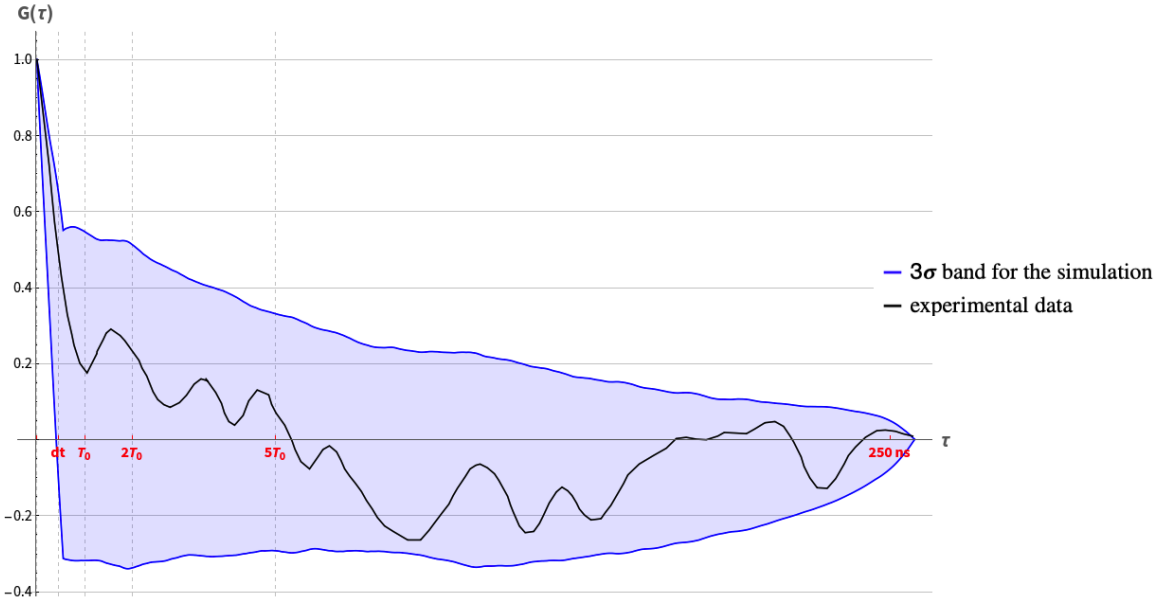

Figure 5.11: PMT voltage's auto-correlation function, for the observation window starting at the 59th cavity round-trip.

5.3.2.2 Observation window starting at the 60th cavity round-trip

If the observation window starts at the 60th cavity round-trip, the degree of photon clustering decreases further. Therefore, the Fano factor becomes more closer to DTMPR curve, as can be seen in Fig. 5.12. The data is inconsistent with the simulation.

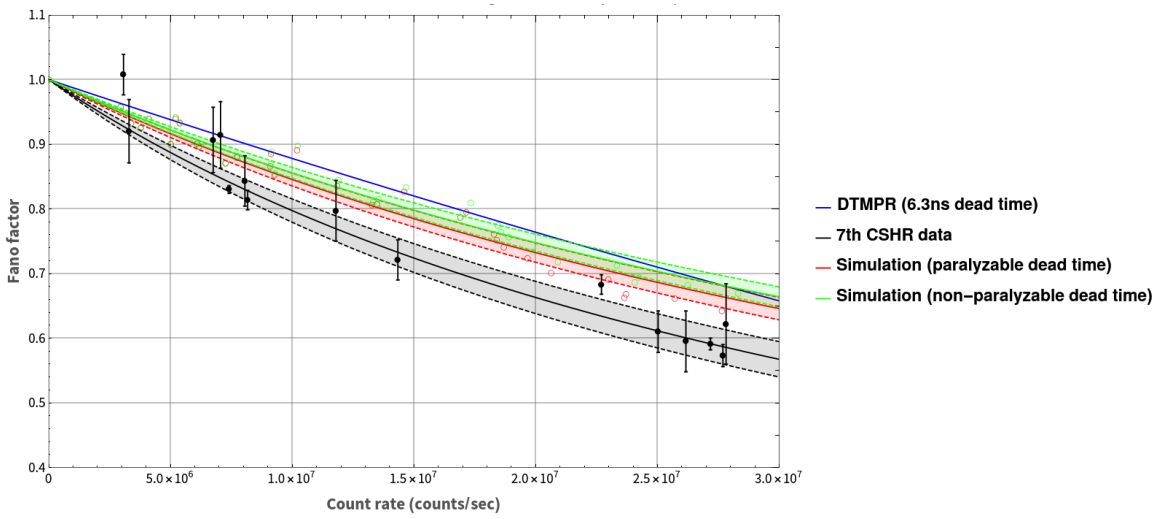

Figure 5.12: Simulated Fano factor, for the observation window starting at the 60th cavity round-trip.

And the simulated auto-correlation function is still in accordance with the observed one as shown in Fig. 5.13.

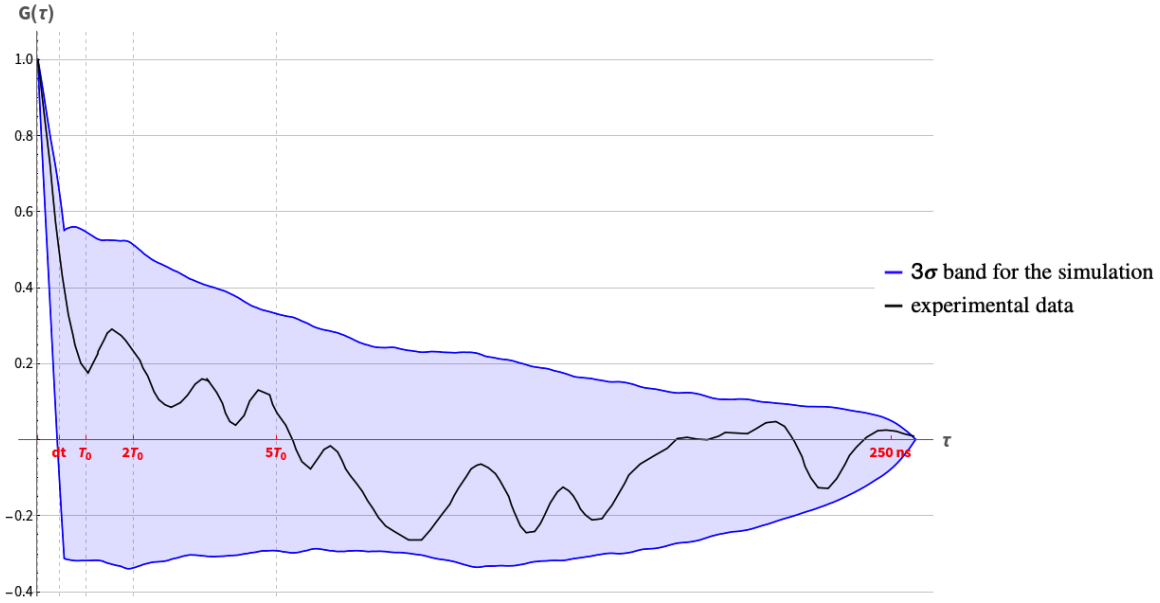

Figure 5.13: PMT voltage's auto-correlation function, for the observation window starting at the 60th cavity round-trip.

5.3.2.3 Observation window starting at the 61th cavity round-trip

If the observation window starts at the 61th cavity round-trip, the degree of clustering decreases further. Therefore, the Fano factor becomes more closer to DTMPR curve, as can be seen in Fig. 5.14.

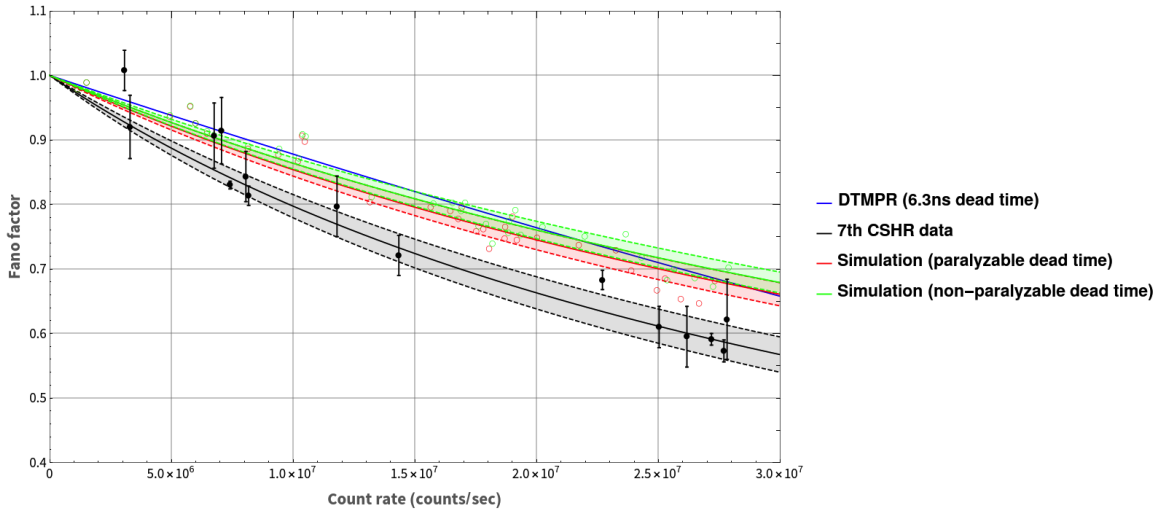

Figure 5.14: Simulated Fano factor, for the observation window starting at the 61th cavity round-trip.

And the simulated auto-correlation function is still in accordance with the observed one as shown in Fig. 5.15.

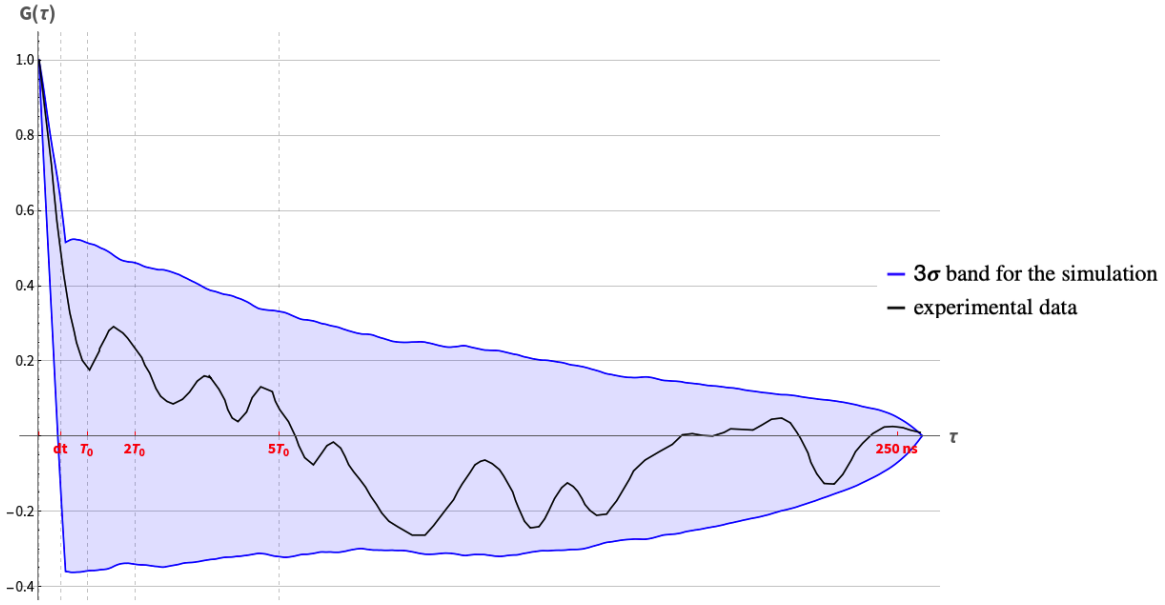

Figure 5.15: PMT voltage's auto-correlation function, for the observation window starting at the 61th cavity round-trip.

5.3.2.4 Observation window starting at the 64th cavity round-trip

As can be seen from Fig. 5.4, the linear increasing trend of the intensity is preserved almost up to the cavity round-trip number of 90. Therefore, for the observation window starting at the 64th cavity round-trip, the linear trend may still hold. And, the degree of photon clustering should be lower compared to the previously investigated observation windows. Therefore, the simulated Fano factor almost converges to DTMPR curve, as can be seen from Fig. 5.16. For the observation window starting at between the 59th and 85th cavity round-trip, the simulated Fano factor may not be compatible with the observed Fano factor.

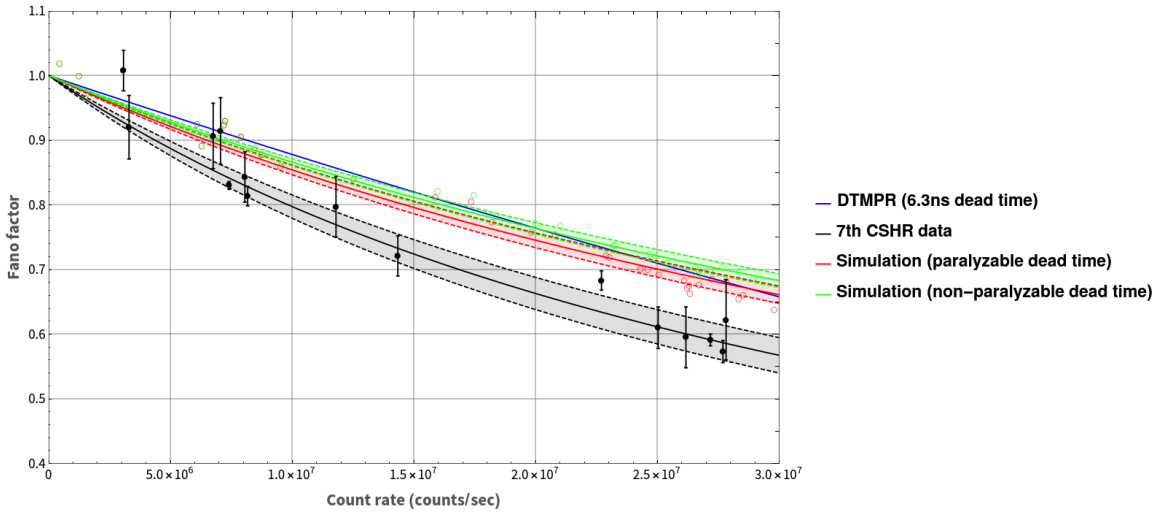

Figure 5.16: Simulated Fano factor, for the observation window starting at the 64th cavity round-trip.

The simulated auto-correlation function is still in accordance with the observed one as can be seen in Fig. 5.17. However, the observed one nearly touches the boundary of 3σ band of the simulation. Considering the previously simulated auto-correlation functions above, we may expect that if the observation window starts later than the 64th cavity round-trip and photon clustering diminishes more, the simulated auto-correlation function starts to contradict the observed one.

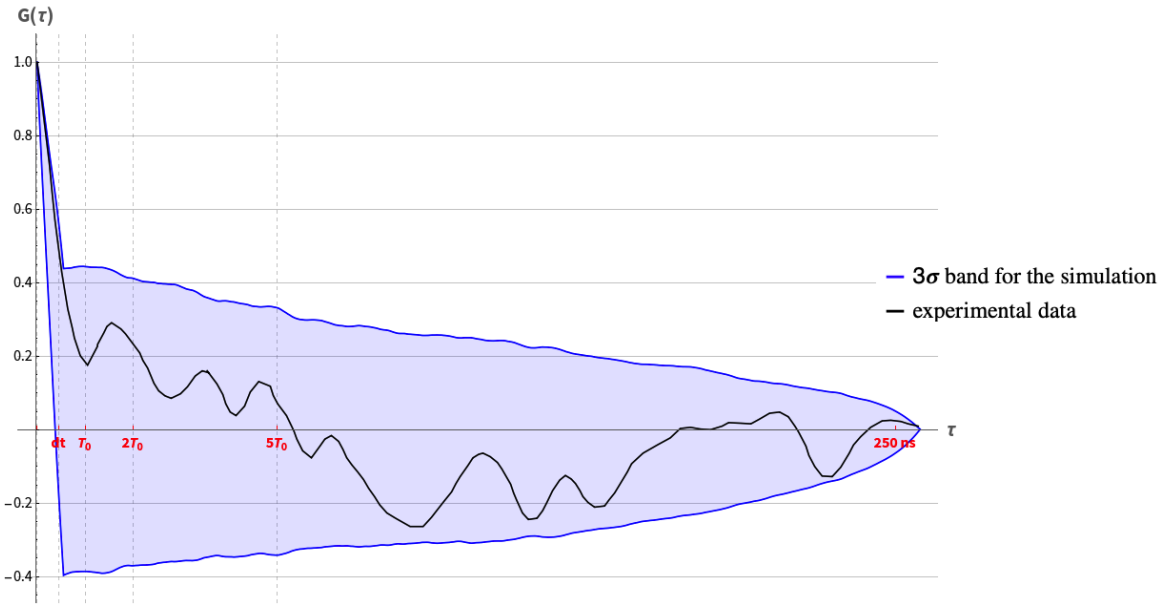

Figure 5.17: PMT voltage's auto-correlation function, for the observation window starting at the 64th cavity round-trip.

5.3.2.5 Observation window starting at the 57th cavity round-trip

Up to now, we have checked the case when the observation window starts at the cavity round-trip number equal to or greater than 58. From now on, we will investigate the case when the observation window starts earlier than the 58th cavity round-trip. Considering the ratio between the fixed step-wise intensity increment to the intensity of the spontaneous emission shown in Fig. 5.6, if the observation window starts at the 57th cavity round-trip, the photon clustering becomes more significant compare to the case of observation window starting at the 58th cavity round-trip. Therefore, reduction of Fano factor becomes more significant, as can be seen from Fig. 5.18. The simulated Fano factor is still in accordance with the data, and the simulated auto-correlation function starts to deviate from the observation, as can be seen from Fig. 5.19.

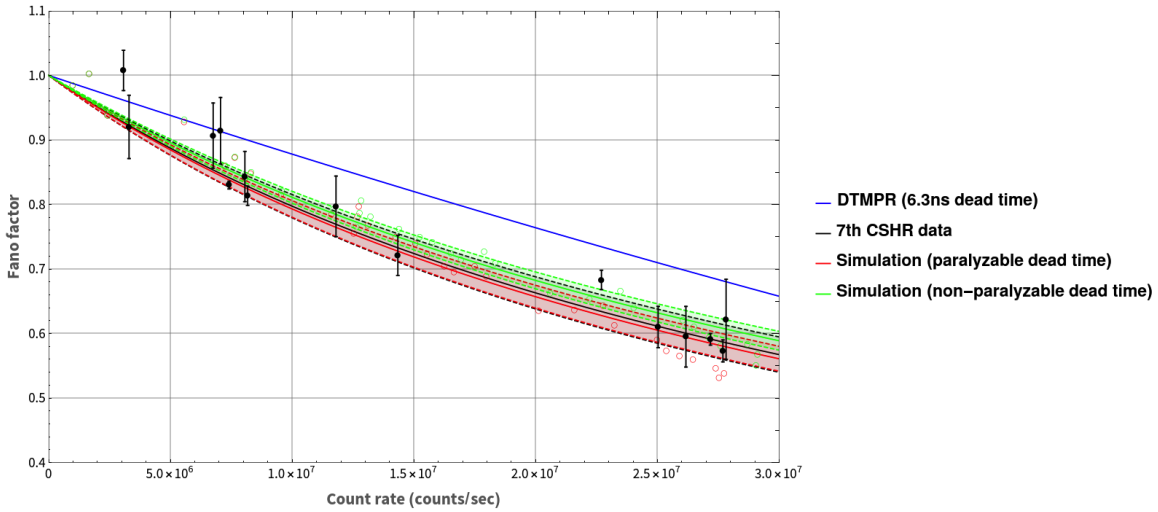

Figure 5.18: Simulated Fano factor, for the observation window starting at the 57th cavity round-trip.

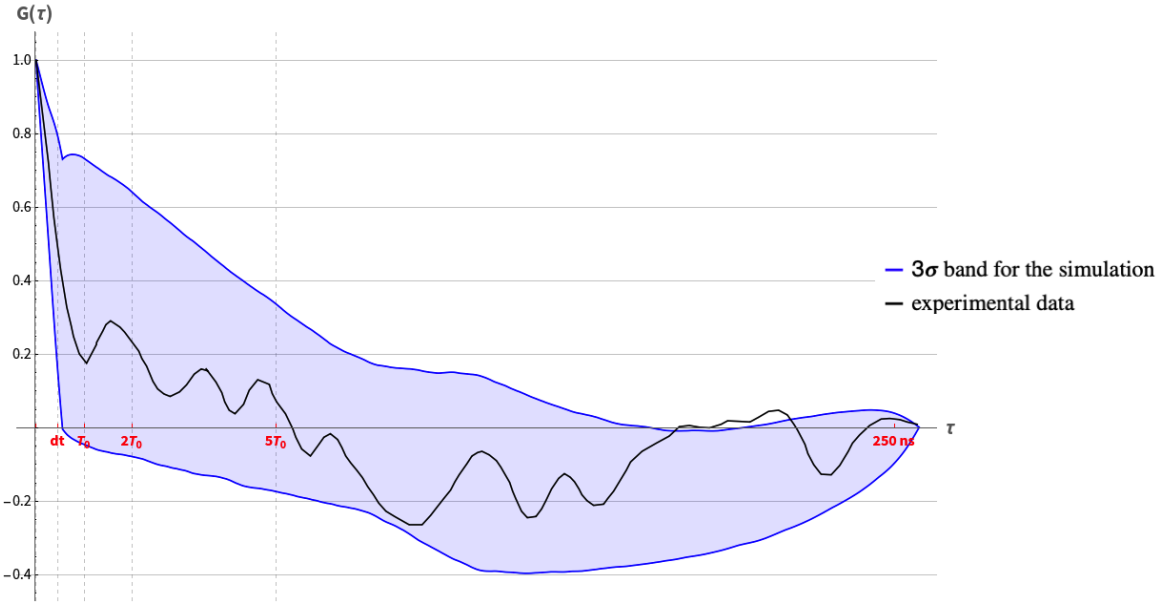

Figure 5.19: PMT voltage's auto-correlation function, for the observation window starting at the 57th cavity round-trip.

5.3.2.6 Observation window starting at the 56th cavity round-trip

If the observation window starts at the 56th cavity round-trip, the simulated Fano factor is in accordance with the data, as can be seen from Fig. 5.20, but the simulated auto-correlation function is inconsistent with the data, as shown in Fig. 5.21.

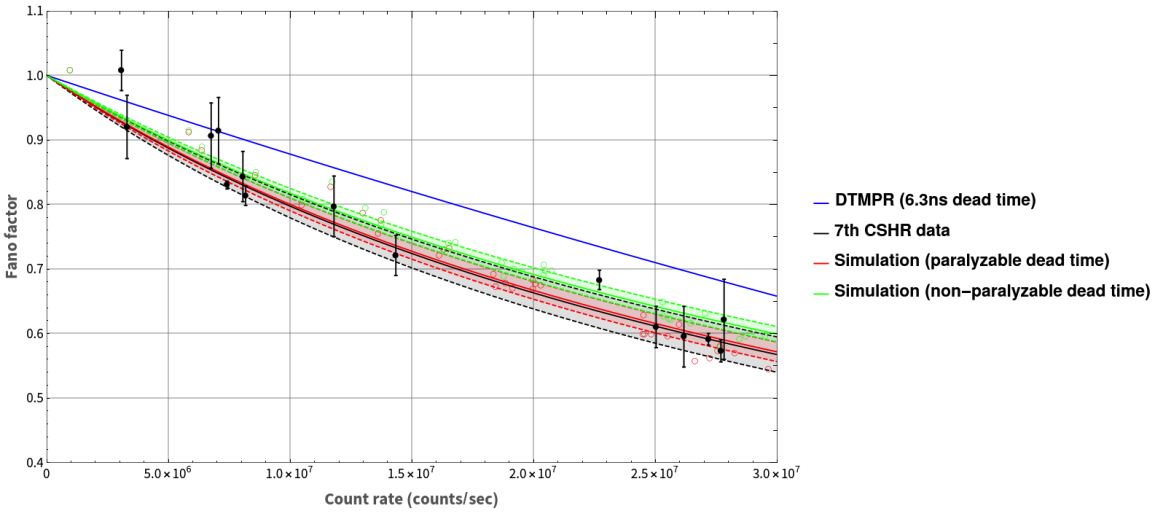

Figure 5.20: Simulated Fano factor, for the observation window starting at the 56th cavity round-trip.

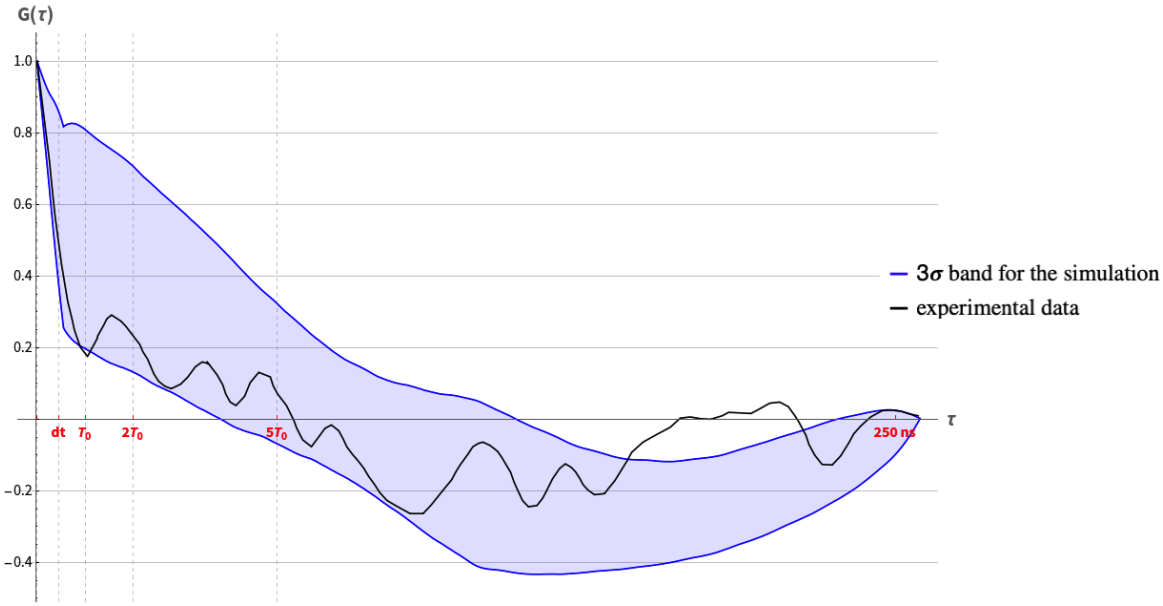

Figure 5.21: PMT voltage's auto-correlation function, for the observation window starting at the 56th cavity round-trip.

5.3.2.7 Observation window starting at the 55th cavity round-trip

If the observation window starts at the 55th cavity round-trip, as the low intensity level from the spontaneous emission is kept for most of the observation window, the degree of photon clustering is reduced compared to the case of observation windows starting at the 56th cavity round-trip. Consequently, the simulated Fano factor is inconsistent with the observed one as can be seen from Fig. 5.22. Also, the simulated auto-correlation function contradicts the observed one as can be seen from Fig. 5.23.

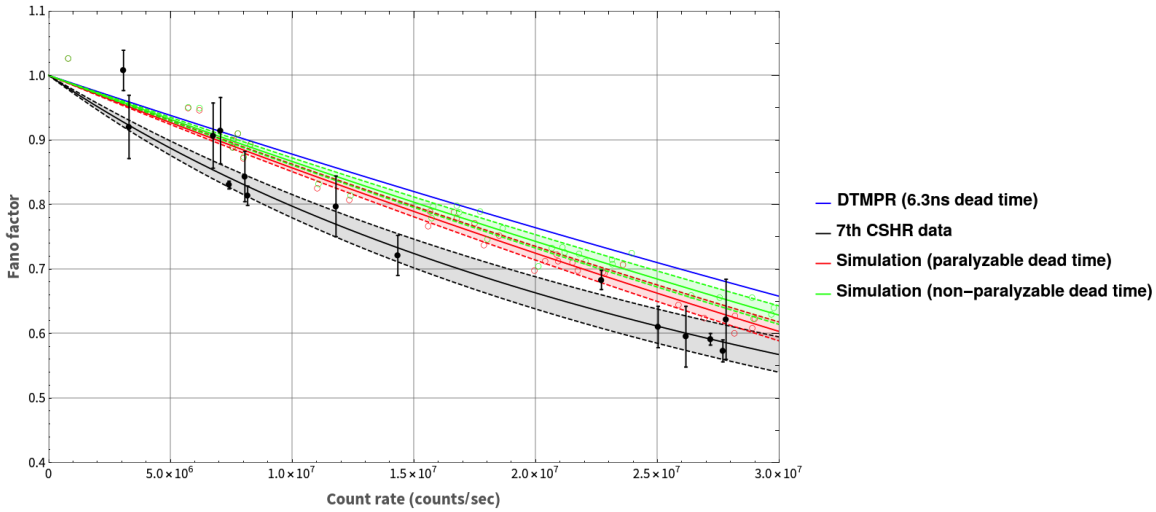

Figure 5.22: Simulated Fano factor, for the observation window starting at the 55th cavity round-trip.

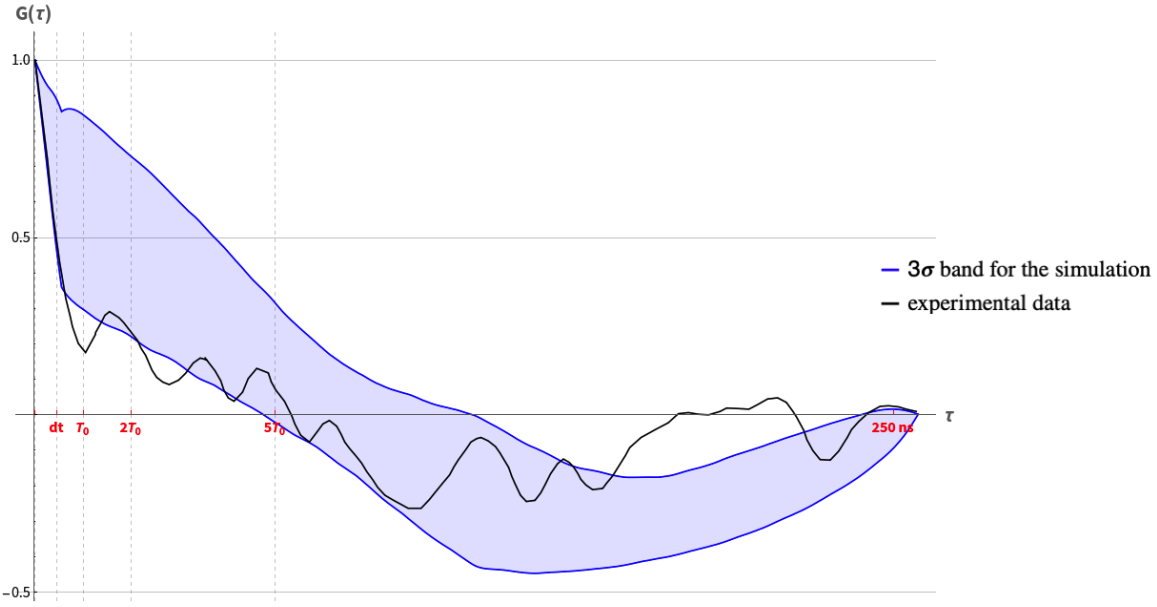

Figure 5.23: PMT voltage's auto-correlation function, for the observation window starting at the 55th cavity round-trip.

5.3.2.8 Observation window starting at the 54th cavity round-trip

If the starting cavity round-trip number of the observation window is further reduced to 54, the photon clustering disappears. Therefore, as can be seen from Fig. 5.24, the simulated Fano factor is consistent with DTMPR curve and cannot explain the observed one. And the simulated auto-correlation function contradicts the observed one as can be seen from Fig. 5.25.

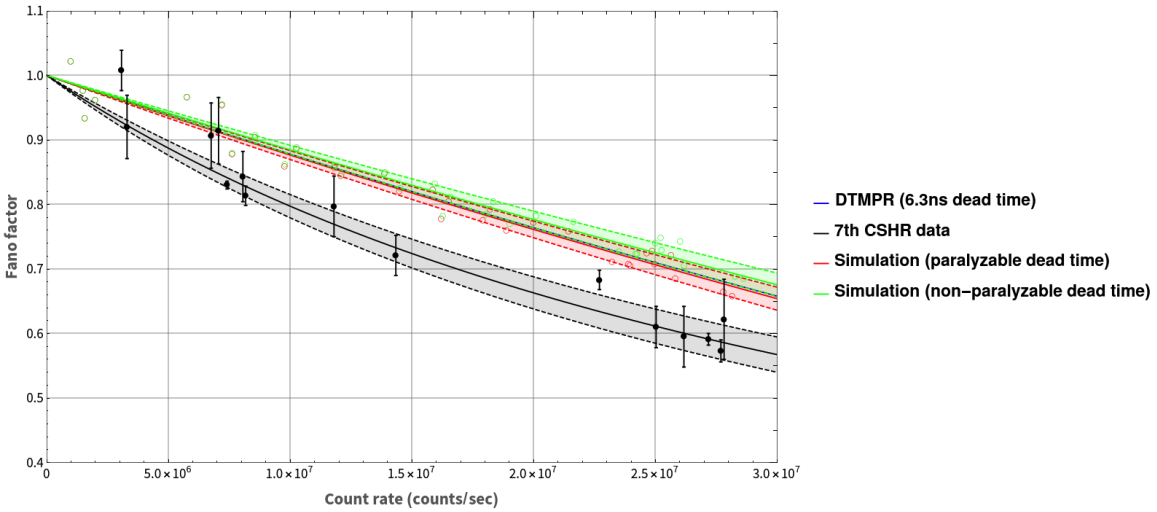

Figure 5.24: Simulated Fano factor, for the observation window starting at the 54th cavity round-trip.

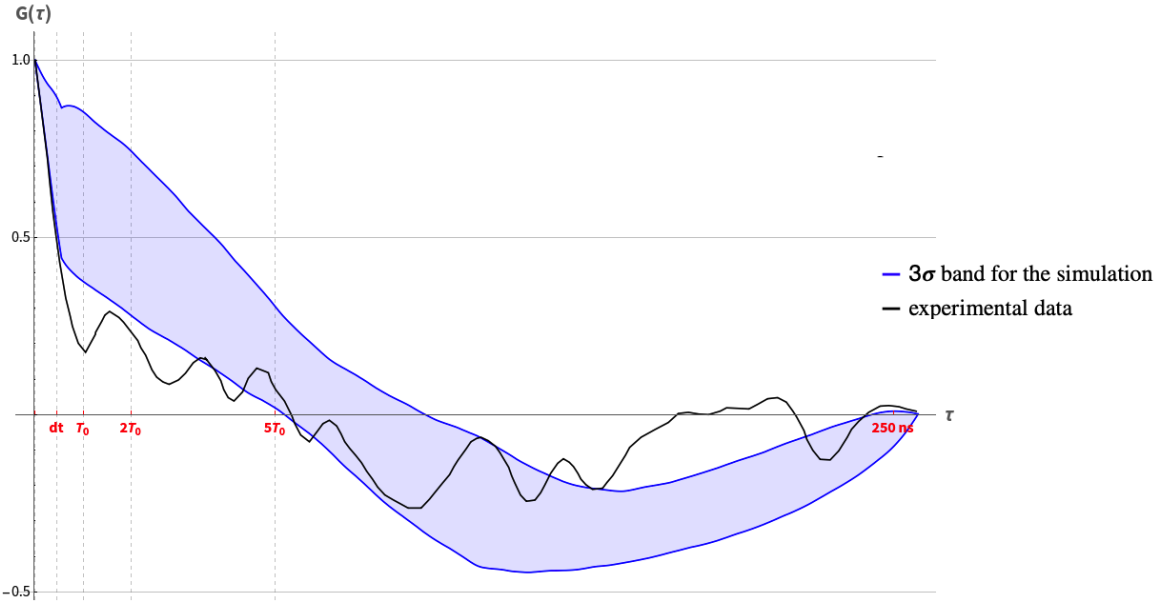

Figure 5.25: PMT voltage's auto-correlation function, for the observation window starting at the 54th cavity round-trip.

Chapter 6

A proposed re-measurement

As shown in Chapter 5, the main difference between Chen-Madey analysis and our study is in the degree of the photon clustering within the observation window. Therefore, to more definitively measure the photon statistics of FEL, a new experiment may be useful. In this chapter, we propose an improved re-measurement.

6.1 Improved strategies of FEL photon counting

6.1.1 Use of a Silicon Photomultiplier

Instead of using a vacuum PMT as done in Chen-Madey experiment, a silicon multiplier (SiPM) can be used for the photon counting experiment in the FEL, which can increase the photon counting's quantum efficiency [35]. Moreover, as a SiPM can be segmented a direct measure of pile-up at higher count rates can be feasible, and it can also determine the number of multiple photons hitting the same photosensor element due to the available quantized pulse amplitudes [35]. Therefore, a more accurate photon counting can be done using a SiPM.

6.1.2 Photo-sensor signal acquisition over the whole macropulse

Rather than doing the gated counting that was done in Chen-Madey experiment, photo-sensor signal over the whole macropulse can be recorded, and then the selection cuts can be made with the information of stored intensity profile of the fundamental mode to count the photons within the observation window, with any decent digitizing oscilloscope, which can be accompanied by cross-checks and internal consistency checks [35]. In this way, we may diminish any measurement errors originating from the use of triggers (e.g., extension of photo-sensor signals over in and out of the gate's boundary).

6.1.3 Superposition of photo-sensor signals from many ensembles

To clarify whether the photon clustering exists over the observation window, the new measurement should include obtaining the superposition of photo-sensor signals over many ensembles, which was not done in Chen-Madey experiment. In this way, we can obtain the intensity profile of Fig. 3.11 to trace the effect of photon clustering on the counted photon number.

6.1.4 Photon counting at different quantum efficiencies

As can be seen from Eqn. (2.44), the observed Fano factor, F_{out}, depends on the quantum efficiency η only if F_{in} differs from unity. Therefore, if the Fano factor is measured at different quantum efficiencies (use of SiPMs of different quantum efficiencies can be a method), we can accurately determine whether F_{in} differs from unity by checking the dependency of F_{out} on η as shown in Fig. 6.1.

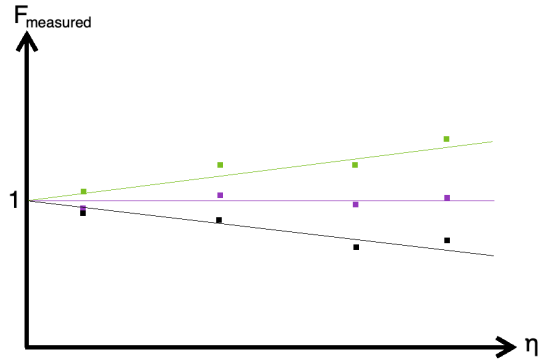

Figure 6.1: Possible correlation between the measured Fano factor and the quantum efficiency.

6.2 Photon count of the fundamental mode

Most of the previous literatures on FEL photon statistics are focused on the fundamental mode. Therefore, photon count at the fundamental mode can yield more physical quantities that can be directly compared to the studies.

The FEL used for the experiment should meet the followings: 1) a proper wavelength of the fundamental mode should be chosen to satisfy large quantum efficiency of the photon counting, and 2) the FEL power should be low enough to insure that the chaotic nature of light and the dead time effect of the photon counting are not significant.

Chapter 7

Conclusion

In this dissertation we investigated the conclusions of claimed non-standard FEL photon statistics from Chen-Madey experiment.

From the available FEL theory, we could not find a reason why the photon statistics observed by Chen and Madey should be sub-Poissonian.

From the re-examination of analysis of Chen-Madey experiment, we found that their photon clustering analysis may not be complete. From our simulation of the photon statistics of Chen-Madey experiment, we find that the observed reduction of Fano factor could be explained within the standard FEL theory if one combines the detector dead time effect with photon clustering arising from the FEL gain. However, we cannot rule out the possibility that the observed reduction of Fano factor arises from a non-standard behavior of FEL either.

As verifying whether the experimental FEL photon statistics is in accordance with the available theory is a very important issue, the proposed new FEL photon counting experiment may be useful. And from an ongoing photon counting experiment of single electron's undulator radiation in the Integrable Optics Test Accelerator in Fermilab [36], the quantum fluctuations of radiation emitted by free-electron may be accurately found, as the classical fluctuations of radiation can be diminished. While the available FEL theory is in consistent with experiment in many aspects so far, the new data of the photon statistics of radiation of free-electrons will be a good indicator of validity of the theory.

We conclude that if a sub-Poissonian light emitted by free-electrons is experimentally observed, contradicting the standard theory, a theory beyond the standard one may be necessary to explain the observation.

Bibliography

[1] J. M. J. Madey. Stimulated Emission of Bremsstrahlung in a Periodic Magnetic Field. *Journal of Applied Physics*, 42(5):1906-1913, 1971.

[2] D. A. G. Deacon, L. R. Elias, J. M. J. Madey, G. J. Ramian, H. A. Schwettman, and T. I. Smith. First Operation of a Free-Electron Laser. *Physical Review Letters*, 38(16):892-894, 1977.

[3] T. Chen and J. M. J. Madey. Observation of Sub-Poisson Fluctuations in the Intensity of the Seventh Coherent Spontaneous Harmonic Emitted by a rf Linac Free-Electron Laser. *Physical Review Letters*, 86(26):5906-5909, 2001.

[4] T. Chen and J. M. J. Madey. Effects of Electron Shot Noise and Quantum Field Fluctuations on the Photon Statistics of the Coherent Spontaneous Harmonic Radiation. *IEEE Journal of Quantum Electronics*, 44(3):294-302, 2008.

[5] M. C. Teich, T. Tanabe, T. C. Marshall, and J. Galayda. Statistical Properties of Wiggler and Bending-Magnet Radiation from the Brookhaven Vacuum-Ultraviolet Electron Storage Ring. *Physical Review Letters*, 65(27):3393-3396, 1990.

[6] I. Lobach, K. J. Kim, T. Shaftan, V. Lebedev, S. Nagaitsev, A. Romanov, G. Stancari, A. Valishev, A. Murokh, A. Halavanau, Z. Huang, and V. Yakimenko. Study of Fluctuations in Undulator Radiation in the IOTA Ring at Fermilab. *Proceedings of 10th International Partile Accelerator Conference*, page 777-780, 2019.

[7] M. Hogan, C. Pellegrini, J. Rosenzweig, G. Travish, A. Varfolomeev, S. Anderson, K. Bishofberger, P. Frigola, A. Murokh, N. Osmanov, S. Reiche, and A. Tremaine. Measurements of High Gain and Intensity Fluctuations in a Self-Amplified, Spontaneous-Emission Free-Electron Laser. *Physical Review Letters*, 80(2):289-292, 1998.

[8] J.-W. Park, K.-J. Kim, and R. R. Lindberg. An Investigation of Possible Non-Standard Photon Statistics in a Free-Electron Laser I: Experiment. *Proceedings of FEL2019*, page 161-164, 2019.

[9] J.-W. Park, K.-J. Kim, and R. R. Lindberg. An Investigation of Possible Non-Standard Photon Statistics in a Free-Electron Laser II: Theory. *Proceedings of FEL2019*, page 165-167, 2019.

[10] K. Kim, Z. Huang, and R. Lindberg. *Synchrotron Radiation and Free-Electron Lasers*, Cambridge University Press, Cambridge, United Kingdom, 1st edition, 2017.

[11] M. S. Fox, *Quantum Optics: An Introduction*, Oxford University Press, Oxford, United Kingdom, 1st edition, 2006.

[12] Fano, U. Ionization Yield of Radiations. II. The Fluctuations of the Number of Ions. *Physical Review*, 72(1):26-29, 1947.

[13] T. Chen. *Photon statistics of coherent spontaneous harmonic radiation of a linac free electron laser*. PhD thesis, Duke university, 1999.

[14] H. Bachor and T. C. Ralph. *A guide to Experiments in Quantum Optics*, Wiley, Weinheim, Germany, 2nd edition, 2004.

[15] R. E. Slusher, L. W. Hollberg, B. Yurke, J. C. Mertz, and J. F. Valley. Observation of Squeezed States Generated by Four-Wave Mixing in an Optical Cavity. *Physical Review Letters*, 55(22):2409-2412, 1985.

[16] R. M. Shelby, M. D. Levenson, S. H. Perlmutter, R. G. DeVoe, and D. F. Walls. Broad-Band Parametric Deamplification of Quantum Noise in an Optical Fiber. *Physical Review Letters*, 57(6):691-694, 1986.

[17] L.-A. Wu, H. J. Kimble, J. L. Hall, and H. Wu. Generation of Squeezed States by Parametric Down Conversion. *Physical Review Letters*, 57(20):2520-2523, 1986.

[18] J. M. J. Madey. Wilson Prize article: From vacuum tubes to lasers and back again. *Physical Review Special Topics - Accelerators and Beams*, 17:074901, 2014.

[19] R. Loudon, *The Quantum Theory of Light*, Oxford University Press, Oxford, United Kingdom, 3rd edition, 2000.

[20] Y. S. Li. Solutions of USPAS Summer 2019 (Introduction to Synchrotron Radiation and FELs), 2019.

[21] R. Bonifacio, N. Piovella, G. R. M. Robb, and A. Schiavi. Quantum regime of free electron lasers starting from noise. *Physical Review Special Topics - Accelerators and Beams*, 9:090701, 2006.

[22] J. Gea-Banacloche. Quantum theory of the free-electron laser: Large gain, saturation, and photon statistics. *Physical Review A*, 31(3):1607-1621, 1985.

[23] W. Becker, M. O. Scully, and M. S. Zubairy. Generation of Squeezed Coherent States via a Free-Electron Laser. *Physical Review Letters*, 48(7):475-477, 1982.

[24] I. Gjaja and A. Bhattacharjee. Generation of squeezed radiation from a free-electron laser. *Physical Review A*, 36(11):5486-5489, 1987.

[25] J. Gea-Banacloche. Steady-state photon statistics of a free-electron laser. *Physical Review A*, 33(2):1448-1450, 1986.

[26] C. C. Gerry and P. L. Knight. *Introductory quantum optics*, Cambridge University Press, Cambridge, United Kingdom, 1st edition, 2005.

[27] G. F. Knoll. *Radiation Detection and Measurement*, John Wiley & Sons, Inc., Hoboken, NJ, United States, 4th edition, 2010.

[28] G. Vannucci and M. C. Teich. Dead-time-modified photocount mean and variance for chaotic radiation. *Journal of the Optical Society of America*, 71(2):164-170, 1981.

[29] W. M. Fawley. *A User Manual for GINGER-H and its Post-Processor XPLOT-GINH, version 2.0k*. Lawrence Berkeley National Laboratory, 2012.

[30] E. Szarmes. *Classical Theory of Free-Electron Lasers*, Morgan & Claypool, San Rafael, CA, United States, 1st edition, 2014.

[31] G. A. Barnett, J. M. J. Madey, C. B. McKee, K. D. Straub, and E. B. Szarmes. The Mark III IR FEL: improvements in performance and operation. *Nuclear Instruments and Methods in Physics Research A*, 375:97-99, 1996.

[32] G. Dattoli, L. Giannessi, A. Renieri, and A. Torre. VI Theory of Compton Free Electron Lasers. *Progress in optics*, 31:321-412, 1993.

[33] D. J. Bamford and D. A. G. Deacon. Measurement of the coherent harmonics emitted in the Mark III free electron laser. *Nuclear Instruments and Methods in Physics Research A*, 285:23-30, 1989.

[34] Y. S. Li, K.-J. Kim, and R. Lindberg. Axial Symmetry in Spontaneous Undulator Radiation for XFELO Two-Bunch Experiment. *Proceedings of FEL2019*, page 134-137, 2019.

[35] G. Varner, private communication.

[36] I. Lobach. Study of Fluctuations in Undulator Radiation in the IOTA Ring at Fermilab. Budker Seminar at Fermilab, 2019. Retrieved November 28, 2019, from https://indico.fnal.gov/event/21018/material/slides/0.pptx.